PITCH AND ALTITUDE CONTROL OF AN UNMANNED AIRSHIP WITH SLIDING GONDOLA

by

Ahmad Alsayed

Thesis submitted in partial fulfillment of the requirements for the

Master of Applied Science in Mechanical Engineering

Ottawa-Carleton Institute for Mechanical and Aerospace Engineering

University of Ottawa

TITLE: Pitch and altitude control of an unmanned airship with sliding gondola

AUTHOR: Ahmad Alsayed

SUPERVISOR: Dr. Eric Lanteigne

NUMBER OF PAGES: xv, 80

Acknowledgements

I would like to express my very great appreciation to Professor Eric Lanteigne, my research supervisor, for his patient guidance, encouragement and useful critiques of this thesis. Also, I would thank my family for their loving support during my study.

Abstract

Alsayed, Ahmad. M.A.Sc University of Ottawa, 2017. *Pitch and altitude control of an unmanned airship with sliding gondola.* Supervised by Dr. E. Lanteigne, Ph.D..

An unmanned airship has an ability of heavy lifting capabilities, low environmental footprint, and long endurance, however, the unmanned airships are faced challenges linked to the maneuverability during landing and the reliability of control. In this thesis, the six degrees of freedom equations of motion of a miniature unmanned airship with a sliding gondola have been derived. Then the model was implemented and simulated in the Matlab/Simulink. The wind disturbance was also implemented in the model. The model was then trimmed and linearized in to obtain pitch and altitude PID controllers using the gondola position as an input. Both controllers were simulated with different reference inputs and disturbances. The experimental platform, hardware, sensors and graphical user interface (GUI) of the ground station were described. Then, experimental flight tests were performed to evaluate the pitch controller.

Table of Contents

List of Tables

List of Figures

List of Symbols

ρ_a	Air density	24
C_{Dho}	Hull zero-incidence drag coefficient	26
C_{Dfo}	Fin zero-incidence drag coefficient	26
C_{DGo}	Gondola zero-incidence drag coefficient	26
C_{Dch}	Hull cross-flow drag coefficient	26
C_{Dcf}	Fin cross-flow drag coefficient	26
C_{DcG}	Gondola cross-flow drag coefficient	26
S_h	Hull reference area	26
S_f	Fin reference area	26
S_G	Gondola reference area	26
n_f	Fin efficiency factor	26
n_k	Hull efficiency factor	26
I_1, I_3, J_1, J_2	Hull integrals	26
$\mathbf{g}$	Gravitational vector expressed in the body frame	25
g	Standard acceleration due to gravity	25
U	Volume of the helium envelope	34
T_R	Right propeller thrust	27
T_L	Lift propeller thrust	27
$d_{G,z}, d_{G,y}$	Normal distance from the right and left propeller center to the gondola center to the x - z plane	27
$\mathbf{F}$	Equations of motion	34
$\mathbf{X}$	State vector	34
$\mathbf{U}$	Input (or control) vector	34
$\mathbf{X_e}$	Equilibrium state or a trim point	34
h	Altitude	34
$\mathbf{X}_{long}$	Longitudinal state vector	36
$\mathbf{y}$	Output vector	36
$\mathbf{C}$	output matrix	36
$\mathbf{D}$	Feedthrough matrix	36
λ	Eigenvalue	37

List of Acronyms

GUI	Graphical user interface	iv
PID	Proportional-integral-derivation	3
DOF	Degree of freedom	7
FCC	Flight Control Computer	10
SISO	Single input single output	11
CFD	Computational fluid dynamics	11
AFSMC	Adaptive fuzzy sliding mode control	11
INDI	Incremental nonlinear dynamics inversion	12
TLC	Trajectory linearization control	12
CV	Center volume	14
CG	Center gravity	14
DCM	Direction cosine matrix	16
LAT	Linear Analysis Tool	35
IMU	Inertial Measurement Unit	54
ESC	Electrical speed controller	54

Chapter 1

Introduction

In the last few decades, several studies have been proposed on unmanned airships. For long duration missions of one day to five days where high speeds are not crucial, airships are seen as suitable vehicles [1]. Airships use a lifting gas to generate lift, therefore, the energy is mostly used to perform attitude and velocity control. They can be classified into three main structural categories: rigid, semi-rigid and non-rigid airships as seen in Figure 1.1. Rigid airships have a rigid structure and non-pressurized gasbag that contains lifting gas. Semi-rigid airships require a pressured gas to maintain the shape, but they have a rigid keel along the bottom of the envelope. Lastly, non-rigid airships or blimps are the most common for smaller sized vehicles [2]. The lifting gas envelope in blimps has an internal overpressure to maintain its shape. The envelope is inflated with the helium to make the airship lighter than the surrounding air. While airships have forward and rear ballonets to maintain the lifting gas pressure constant with altitude changes and to control the pitch angle, smaller vehicles must rely on thruster forces to change altitude.

1.1 Motivation

Smaller blimps typically cannot be equipped with ballonets for altitude and pitch control due to the lower lifting gas buoyancy to payload ratio. The stricter weight restrictions reduce the number of ancillary components permissible. As a consequence, smaller lighter than air unmanned vehicles must rely on other means of controlling their attitude and altitude. Different small airships have been proposed. Tri-Turbofan has two thrusters oriented along the longitudinal axis for forwarding motion and a single thruster oriented along the vertical axis of the airship for altitude control [4]. In [5], the vertical thruster of the Tri-Turbofan was replaced with different motor and bigger propeller blade to have enough power to control altitude. Lanteigne et al.

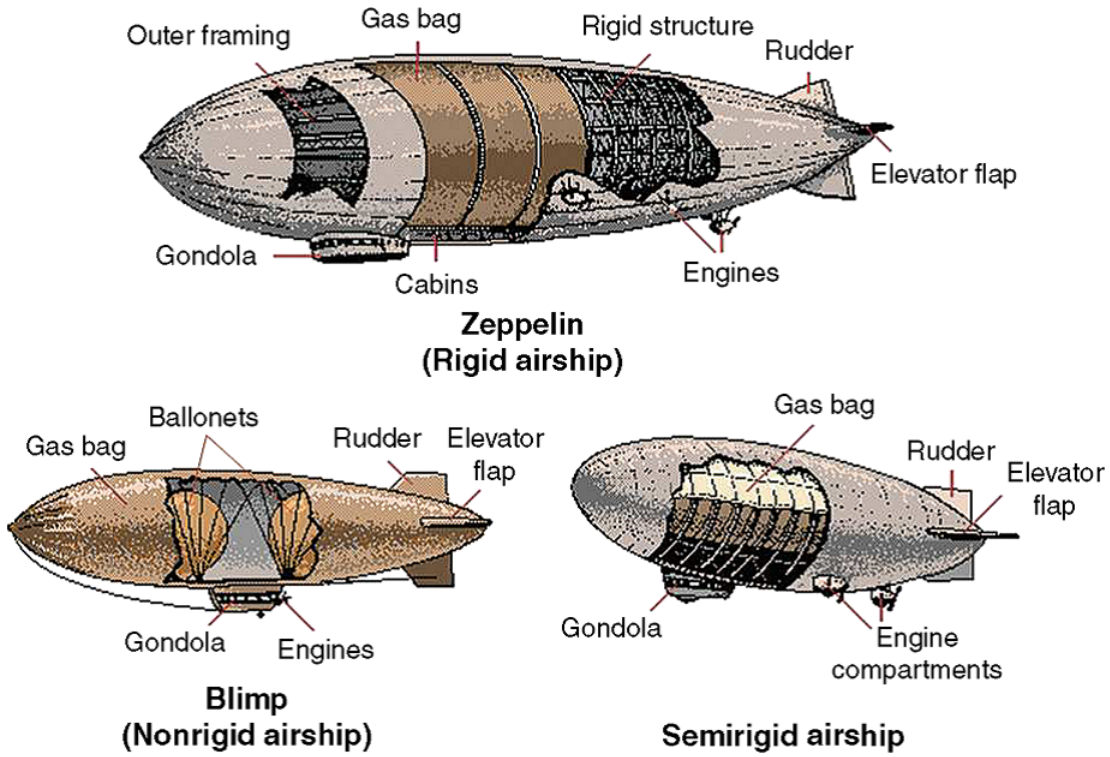

Figure 1.1: Airship Structural categories [3]

provided an alternative to over-actuation and ballonets for the rapid altitude changes required when landing or avoiding obstacles [6]. The proposed design was inspired by the concept center of gravity control, and the design was examined the theoretical and experimental differences between altitude and pitch variations generated using aerodynamic control surfaces (elevator) versus payload repositioning in airships.

1.2 Problem statement and contributions

The research platform that developed by Lanteigne demonstrated that large pitch angle could be reached, and linear flights were possible using the gondola (or payload) as a move to control the pitch angle. This is shown in Figure 1.2. The goal of this thesis is to develop closed-loop controllers for the airship pitch angle and altitude using the gondola position along the keel of the helium envelope as a control input. The sliding gondola provides an alternative to over-actuation and ballonets for the rapid altitude changes required when landing or avoiding obstacles. Both controllers

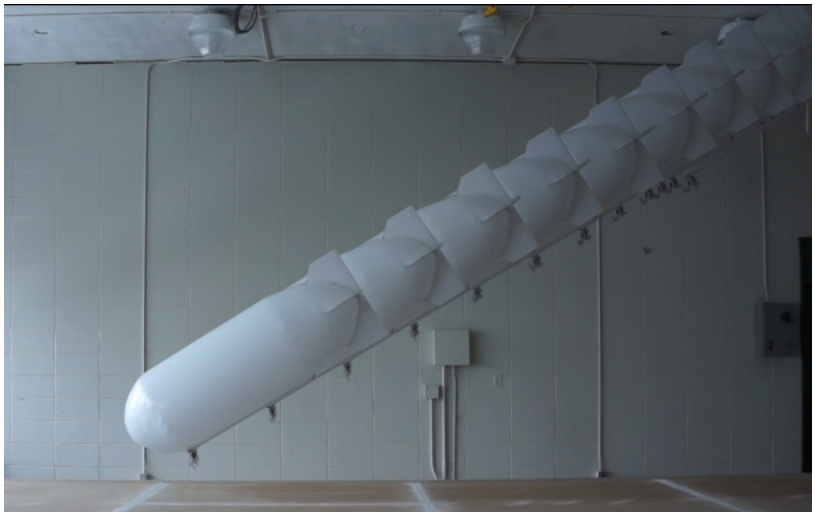

Figure 1.2: Lanteigne's model [6].

were simulated with and without wind disturbances. The airship was able to follow the pitch and altitude reference inputs using the obtaining controllers. A third controller was designed to respect the capabilities of the experimental platform using the gondola speed as the controller output, noises as vibrations, and discrete sampling rate to minimize the ground station platform limitations. The pitch controller was implemented in a graphical user interface for the flight test. Successful flight tests were contributed to the development and validation of the pitch controller. The work was also published in 2017 International Conference on Unmanned Aircraft Systems (ICUAS)[7].

1.3 Thesis structure and content

A review of existing airship models and controls is provided in Chapter 2. The derivation of the equations of motion for the proposed airship is outlined in Chapter 3. The six degrees of freedom model is then implemented in the Simulink environment with the wind disturbance. In Chapter 4, the equations of motion are trimmed and linearized at an operation point which is used to obtain the transfer function equations between inputs and outputs. The PID controllers for the airship pitch angle and altitude are then discussed. Simulations for the closed-loop are illustrated with different reference input types for the controller with and without wind disturbance.

In Chapter 5, the hardware, and software developed for the tests are described, and the flight test results are presented in Chapter 6. Lastly, Chapter 7 presents the overall conclusions of the thesis as well as recommendations for the future work.

Chapter 2

Literature Review

Unmanned airships can be used for several purposes such as wildlife monitoring, security missions, and civil safety [8]. They have low noise, minimizes disturbance to the environment. Unmanned and autonomous airships are mostly smaller than cargo and passenger transportation airships. Therefore they are more affected by atmospheric disturbances such as wind gusts and thermals. Recent advances in design have improved vehicle capitulates. As an example, the Prince Sultan advanced technology research institute recently this year launched a surveillance airship that can fly for 14 days at a height of up to 2000 feet [9].

Airship landing is also a key area of interest with these vehicles. Airlander 10 is the largest aircraft with lighter than air technology that can stay airborne for up to five days manned and over 14 days unmanned [10]. On 24th of August 2016, Airlander undertook a second successful flight test. During the landing, a technical issue led to a heavy landing that resulted in a damaged cockpit as seen in [11], Figure 2.1. In order to accurately predict the capabilities of any vehicle, a detailed dynamic model must be developed and studied.

Figure 2.1: Airlander 10 crashing into the ground during landing [12]

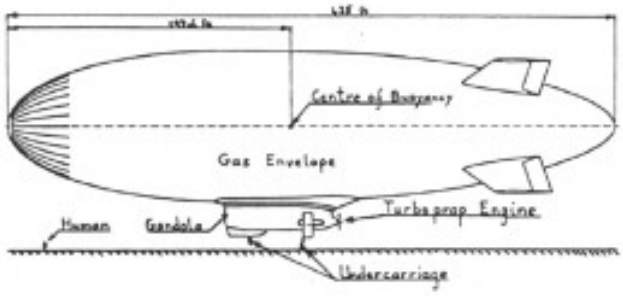

Figure 2.2: YEZ-2A airship [13]

2.1 Airship dynamic modelling

Numerous of airship dynamics models are presented in the literature. Airships are modeled as a rigid-body with three translation and three rotation degree of freedoms which are six differential equations of motion [2]. The following section describes the several different dynamic models developed specifically for airships.

YEZ-2A airship

Gomes [13] developed the first known nonlinear dynamic model for an airship derived based on a Newton-Euler approach for YEZ-2A airship shown in Figure 2.2. The airship has a length of 129.5 m and a total envelope volume of 70.8×10^3 m^3. Moreover, wind tunnel tests were used to obtain the aerodynamic coefficient to run flight dynamic simulation. Subsequently, Sebbane [3] obtained the Newton-Euler and Lagrange Approaches for the same airship. The advantage of the Lagrangian approach is to deal with two scalar energy functions, kinetic and potential energy, while the Newtonian approach is vector oriented. The Lagrangian description uses generalized coordinates (one for each degree of freedom), all of which must be independent [3]. The aerodynamic parameters of the model in [14] are taken from the geometrical configuration of the airship instead of wind tunnel test setup. The authors then derived a computer simulation algorithm for the open-loop simulation. The algorithm was described by simulating a typical airship design and validated again the wind tunnel test results of the YEZ-2A airship.

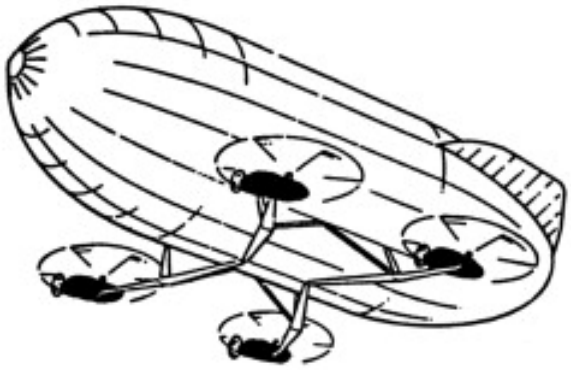

Figure 2.3: Hybrid heavy lift airship [15]

Hybrid heavy-lift airship

NASA, cooperatively with Systems Technology, Inc., presented a study of a hybrid heavy-lift airship as shown in Figure 2.3. The airship has a length of 240 m and a volume of 42475 m^3 [15]. The airship consisted of a helium-filled envelope attached on a platform with a helicopter at each corner [16]. Tischler et al. [17] developed a nonlinear, multi-body, sex DOF digital simulation program named HLASIM to study the dynamic and control of the heavy lift airship. Also, Tischler et al. studied the effects of atmospheric turbulence on the same airship [18]. This type of airship has different flight characteristic because of the aerodynamic lift from the helicopters [16]. Nagabhushan and Tomlinson [15] studied the performance, stability and control properties of the Hybrid heavy lift airship. The study showed five characteristic response modes of the unloaded vehicle; surge subsidence (stable), heave subsidence (stable), pitch oscillation (stable), coupled sway-yaw (unstable) and roll oscillation (stable). The pitch and unstable sway-yaw modes were further destabilized with increasing axial flight speed.

Skyship-500

The airship has a length of 52 m and a volume of 5153.7 m^3 [19]. Amann [20] adapted a six degree of freedom nonlinear flight dynamic simulation program to be applied on the non-rigid Skyship-500 airship, shown in Figure 2.4, using the aerodynamic estimation

Figure 2.4: The Skyship-500 airship [16]

techniques that are obtained by Jones and DeLaurier [21]. The simulation performed well in a wide variety of maneuvers of different control inputs. Li and Nahon [22] further incorporated the flight mechanics, aerostatics and aerodynamics into the same nonlinear airship model then proposed a comparison between the simulation and flight test results for different control inputs. The results of this study demonstrated that the dynamics simulation gives a reasonable estimation of the flight behavior. Jex and Gelhausen [23] adapted the HLASIM simulation program to the study the flight behavior of the Skyship-500. By using a frequency-domain fitting technique, they were able to refine their dynamics model and improved the estimates of the aerodynamic derivatives. In [2], a dynamics modelling and simulation of flexible airship are proposed for Skyship-500 airship. The results show that the airship is not susceptible to aeroelastic instability in its operating range. However, the effects of flexibility on the very thin films should be considered since the films lead to much lower bending stiffness than the conventional airship envelopes.

Due to their large volume and low density, airships that fly outdoor can be strongly affected by atmospheric turbulence like wind gusts. Thomasson [24] derived the non-linear equations of motion of the airship for the case where the fluid mass is acceleration and contains velocity gradients. Azinheira et al. [25] added wind-force and torque to the airship equations of motion. Then, the contribution of the longitudinal and lateral dynamics of the airship motion was analyzed. A real model of an airship was tested in a given range of wind speed and a constant low airspeed which showed

Figure 2.5: Tri-Turbofan has two thrusters oriented along the longitudinal axis for forwarding motion and a single thruster oriented along the vertical axis of the airship for altitude control [4].

how the wind-induced forces do affect the damping of the oscillatory modes. A high-fidelity mathematical model in [26] has been developed to accurately represent the behavior of the airship under the effect of winds and other disturbances. The study showed that the airship cannot maintain stable flight in open-loop however the vehicle can be stabilized using five PID controllers for attitude and altitude using the thrusters.

Tri-Turbofan, Figure 2.5, is a small airship with a single thruster oriented along the vertical axis for altitude control. Frye et al. [4] developed a sex DOF equations of motion for the Tri-Turbofan airship using Newton-Euler approach. The model was integrated into Matlab/Simulink for simulation which allows for flight test analysis, nonlinear simulation, linear simulation and controller integration.

2.2 Airship control

Airships are typically under-actuated systems because they have fewer inputs than degrees of freedom to be controlled. In many studies like in [27, 28, 29], the small under-actuated airships have two vector propellers below the envelope for the thrust, rudders control the yaw movement, and two elevators control the pitch and roll moment, Figure 2.6. These vectored propellers can rotate around their vertical axes to provide a pitching moment. In [4, 5], the airship has a single thruster oriented along

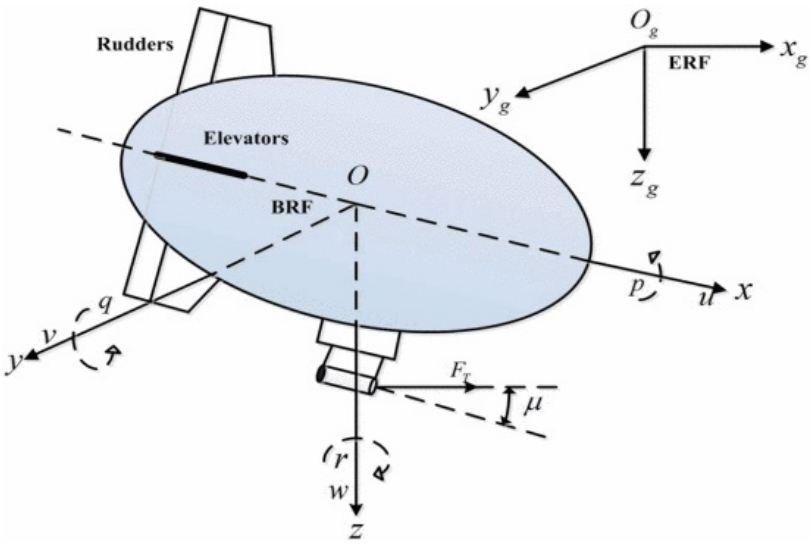

Figure 2.6: The under-actuated airship diagram [27].

the vertical axis for altitude control, and the two main thrusters do not rotate such as in Figure 2.5.

There are numerous different control methods have been proposed and tested specifically for autonomous airships. Generally speaking, the control methods implemented on airship can be classified into linear and nonlinear controllers. Cook in [30] decoupled Gomes model for YEZ-2A airship into longitudinal and lateral motion, and linearized them about a trimmed flight condition. The resulting equations were written in state space form to test the flight stability at different speeds.

A classical PID control algorithm was used by Hong et al. [31] to design an autopilot for trajectory line tracking and altitude hold modes for unmanned airship at low speed and wind disturbance. A Flight Control Computer (FCC) was implemented to calculate the attitude, various flight status, and navigation data during the flight test. The heading response in the flight test was in good agreement with the simulation results while the pitch response of the flight test was exhibited more oscillations than predicted. Adamski et al. [32] showed a simple PD controller for the AS5OO airship. The study showed that it was possible to control the airship flight without using the tail control surfaces in case of unpredictable environmental conditions, namely using engines only. The simulation tests showed small position error in comparison with

the length of the realized trajectory. As a result, the control algorithm possible to be implemented in the physical flight test. The authors in [33] proposed a Simulink-based control system development environment for Project AURORA's unmanned robotic airship. Three SISO controllers were developed; PID controller for velocity, PD controller for altitude and PD controller for heading. The simulation includes autonomous take-off, cruise flight with and without the wind, turning, hovering, and a vertical landing.

A backstepping controller was proposed by Azinheira et al [34] for the path-tracking of an autonomous underactuated airship. This controller is designed from the airship nonlinear dynamic model including wind disturbances, and further enhanced to consider actuators saturation. Recoskie [35] compared backstepping and PID controllers for an airship for a full planner trajectory in the case of an unknown gust. The wind consists of a steady component that was obtained based on CFD analysis and a gust component that was generated by a Dryden filter. The controllers' parameters were tuned manually to reduce tracking error and fuel consumption. The backstepping controller in his study was shown to have a 50% decrease in tracking error and a 40% increase in fuel consumption versus PID controller. Liesk et al. [36] discussed the design of a combined backstepping/Lyapunov controller for the attitude, velocity and altitude control of an unmanned, unstable, fin-less airship. The control law developed provides attitude and velocity control for the entire airship flight regime. The controller includes detailed modelling of sensor noise, computational delays, and actuation dynamics, and it performs well both in simulation and flight tests.

Yang et al [37] present an adaptive fuzzy sliding mode control (AFSMC) for a robotic airship. The AFSMC is proposed to design the attitude control system of the airship, and the global stability of the closed-loop system is proved by using the Lyapunov stability theorem. Moreover, Yang et al. [38] proposed an attitude control scheme for a station-keeping airship using feedback linearization and fuzzy sliding mode control.

A nonlinear control strategy using a Robust Control Lyapunov function was proposed by Kahale et al. [39] to stabilize an airship in the presence of unknown wind

gust. The controller had a well performance to follow a trajectory even in the unknown wind gusts. In [40] the incremental nonlinear dynamics inversion (INDI) system was addressed to provide a lateral control of DRONI airship where the airship is underactuated with an uncertain dynamics model. The model successfully achieved the system desired behavior while neglecting important parameters such as the state-only dependent aerodynamic coefficients, mass, and inertia. A sensor-based control solution was proposed with the simulation results in the case of wind disturbances and a path following loop. The approach showed a combination of a mathematical simplicity with the formulation that allows the application of classical control tools.

The study in [40] proposes a scheme for horizontal position control during the ascent and descent of a stratospheric airship that combines flight dynamics with the thermal model as the pressure and the temperature are changing while the altitude is changing. Altitude is controlled by the thrust or the pitch where the pitch angle is determined by ballonets and an elevator. Zheng et al. [41] present a trajectory tracking control method for an underactuated stratospheric airship based on the trajectory linearization control (TLC) theory. Recently, Fedorenko and Krukhmalev [42] presented an automatic control system for indoor autonomous mini-airship from ground control station by using a cost-effective indoor navigation system. However, there are remain many technical challenges to controlling airships such as obtaining a precise dynamic model, low weight, higher performance avionics, and accurate sensing [43].

The airship in this thesis will be derived using a six DOF nonlinear model originally derived by Gomes [13] and then modified by Lanteigne et al. [6]. The goal of this thesis is to develop and test the first closed-loop controller for the vehicle produced by Lanteigne et al. [6]. To achieve this goal, new hardware and software are designed and tested. They are described in Chapter 5 and 6.

PID controllers were used exclusively in many studies such a [8, 44, 45, 46]. The studies designed the PID controller at zero pitch angle and then tested the controllers at different reference inputs as this is the most continues operation condition. In [8], the PID and the nonlinear controller tracked the desired pitch angle with a maximum error of three degrees however the pitch angle exhibit a high-frequency oscillation with

an amplitude of about two degrees under the PID controller. Using similar linearization control methods, altitude and pitch closed-loop controllers will be simulated and tested under wind and noise disturbances.

Chapter 3

Airship model

3.1 Introduction

The airship in this thesis is modeled using a sex DOF nonlinear model originally derived by Lanteigne et al. [6] for the specific design shown in Figure 3.1 and 3.2.

Two assumptions were made at the outset for practical reasons [47]:

1. The airship forms a rigid body such that aeroelastic effects can be ignored.
2. The airframe is symmetric about the x - z plane such that both the center volume CV and the center gravity CG lie in the plane of symmetry.

These assumptions were justified by the fact that:

1. The envelope is pressurized.
2. The gondola is centered along the rail.

The open-loop trajectories original obtained by Lanteigne et al. were confirmed then wind disturbances were added to evaluate and estimate the performance of the vehicle.

3.2 Kinematics

The position and orientation of the airship can be defined in either the ground $\mathbf{R_g}$ or body (vehicle) $\mathbf{R_v}$ reference frames. The body reference frame $\mathbf{R_v}$ are made at the center of volume CV of the airship as seen in Figure 3.2. Defining the origin of the $\mathbf{R_v}$ at the CV can simplify the computation for the additional mass terms since the center of gravity changes during the flight [48]. Euler angles, Direction cosines, and quaternions can describe finite rotations between frames.

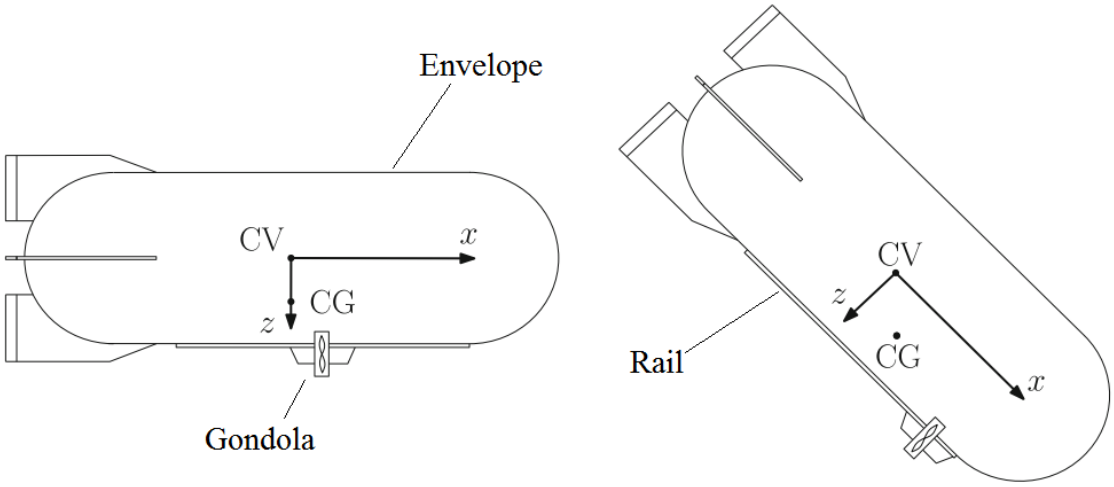

Figure 3.1: Sliding ballast and gondola of a semi-rigid airship concept. The gondola moves along the rail of the vehicle to alter the pitch [6]

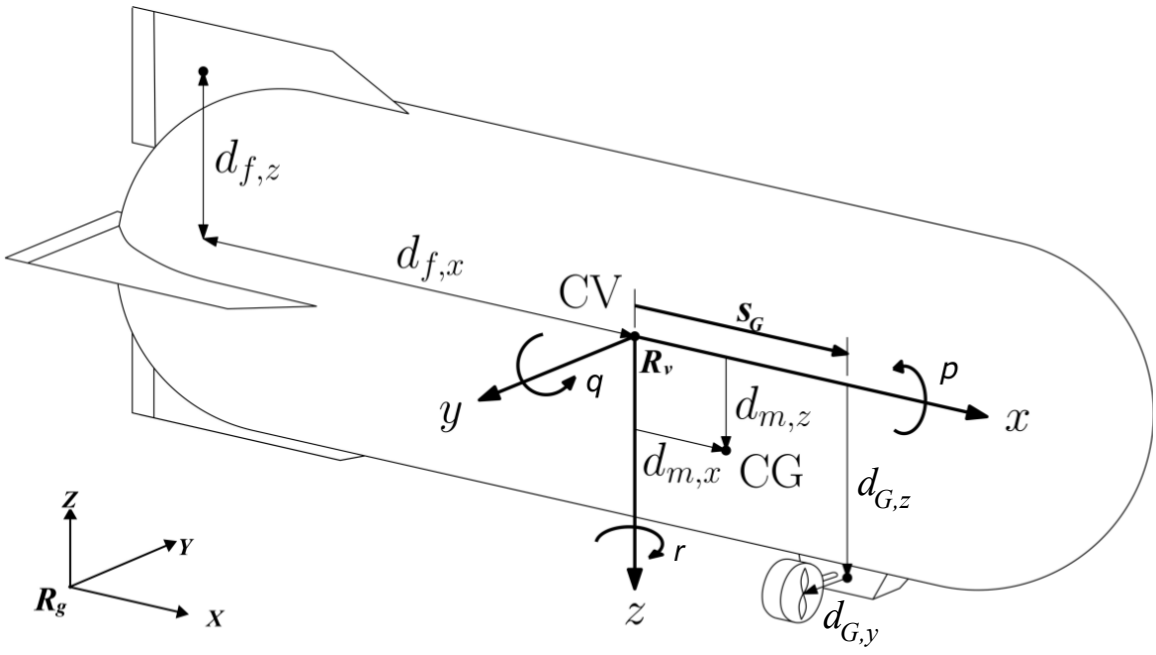

Figure 3.2: Airship model [6]

3.2.1 Euler angles

A 3 x 3 direction cosine matrix (DCM) (of Euler parameters) is used to describe the orientation between the body frame $\mathbf{R_v}$ with respect to the fixed ground frame $\mathbf{R_g}$. The rotations are describe by a roll (ϕ) rotation, followed by pitch (θ) rotation and finally a yaw (ψ) rotation. The angles can be directly measured by the attitude sensors.

The rotation matrix [3] can be written as a function of ϕ, θ and ψ given by:

$$\boldsymbol{\lambda}_1 = \boldsymbol{R_z}(\psi)\ \boldsymbol{R_y}(\theta)\ \boldsymbol{R_x}(\phi) \tag{3.1}$$

with

$$\boldsymbol{R_x}(\phi) = \begin{bmatrix} 1 & 0 & 0 \\ 0 & \cos(\phi) & -\sin(\phi) \\ 0 & \sin(\phi) & \cos(\phi) \end{bmatrix} \tag{3.2}$$

$$\boldsymbol{R_y}(\theta) = \begin{bmatrix} \cos(\theta) & 0 & \sin(\theta) \\ 0 & 1 & 0 \\ -\sin(\theta) & 0 & \cos(\theta) \end{bmatrix} \tag{3.3}$$

$$\boldsymbol{R_z}(\psi) = \begin{bmatrix} \cos(\psi) & -\sin(\psi) & 0 \\ \sin(\psi) & \cos(\psi) & 0 \\ 0 & 0 & 1 \end{bmatrix} \tag{3.4}$$

This transformation is the direction cosine matrix (DCM), and can be written as:

$$\boldsymbol{\lambda}_1 = \begin{bmatrix} \cos\theta\cos\psi & \sin\phi\sin\theta\cos\psi - \cos\phi\sin\psi & \cos\phi\sin\theta\cos\psi + \sin\phi\sin\psi \\ \cos\theta\sin\psi & \sin\phi\sin\theta\sin\psi + \cos\phi\cos\psi & \cos\phi\sin\theta\sin\psi - \sin\phi\cos\psi \\ -\sin\theta & \sin\phi\cos\theta & \cos\phi\cos\theta \end{bmatrix} \tag{3.5}$$

The vehicle's position expressed in the ground frame $\mathbf{R_g}$ is:

$$\mathbf{x} = [x \quad y \quad z \quad | \quad \phi \quad \theta \quad \psi]^{\mathrm{T}} \tag{3.6}$$

where x, y and z are the body frame $\mathbf{R_v}$ origin position with respect to ground frame $\mathbf{R_g}$, and ϕ, θ and ψ are Euler angles corresponding to roll, pitch and yaw, respectively.

The airship's velocity expressed in the ground frame $\mathbf{R_g}$ is:

$$\dot{\mathbf{x}} = [\dot{x} \quad \dot{y} \quad \dot{z} \quad | \quad \dot{\phi} \quad \dot{\theta} \quad \dot{\psi}]^{\mathrm{T}} \tag{3.7}$$

The airship's velocity expressed in the body frame $\mathbf{R_v}$ is:

$$\dot{\mathbf{x}}_v = [u \quad v \quad w \quad | \quad p \quad q \quad r]^{\mathrm{T}} \tag{3.8}$$

The kinematic relationship between the different velocities are given by:

$$\dot{\mathbf{x}} = \begin{bmatrix} \dot{x} \\ \dot{y} \\ \dot{z} \\ \dot{\phi} \\ \dot{\theta} \\ \dot{\psi} \end{bmatrix} = \begin{bmatrix} \boldsymbol{\lambda}_1 & 0_{3\times3} \\ 0_{3\times3} & \boldsymbol{\lambda}_2 \end{bmatrix} \begin{bmatrix} u \\ v \\ w \\ p \\ q \\ r \end{bmatrix} \tag{3.9}$$

where $\boldsymbol{\lambda}_1$ is the rotation matrix defined by Equation 3.5 and $\boldsymbol{\lambda}_2$ is defined by:

$$\boldsymbol{\lambda}_2 = \begin{bmatrix} 1 & 0 & -\sin(\theta) \\ 0 & \cos(\phi) & \sin(\phi)\cos(\theta) \\ 0 & -\sin(\phi) & \cos(\phi)\cos(\theta) \end{bmatrix}^{-1} = \begin{bmatrix} 1 & \sin(\phi)\tan(\theta) & \cos(\phi)\tan(\theta) \\ 0 & \cos(\phi) & -\sin(\phi) \\ 0 & \frac{\sin(\phi)}{\cos(\theta)} & \frac{\cos(\phi)}{\cos(\theta)} \end{bmatrix} \tag{3.10}$$

This matrix presents a singularity for $\theta = \pm\frac{\pi}{2}$, however, this is not likely to be encountered during operation of the airship.

3.2.2 Quaternions

Quaternions are used instead of the Euler angles for attitude representation to avoid the singularity.

The follow matrix is used to convert Euler angels, (ϕ, θ, ψ), to quaternion;

$$\begin{aligned} \begin{bmatrix} q_0 \\ q_1 \\ q_2 \\ q_3 \end{bmatrix} &= \begin{bmatrix} \cos(\frac{\psi}{2}) \\ 0 \\ 0 \\ \sin(\frac{\psi}{2}) \end{bmatrix} \begin{bmatrix} \cos(\frac{\theta}{2}) \\ 0 \\ \sin(\frac{\psi}{2}) \\ 0 \end{bmatrix} \begin{bmatrix} \cos(\frac{\phi}{2}) \\ \sin(\frac{\phi}{2}) \\ 0 \\ 0 \end{bmatrix} \\ &= \begin{bmatrix} \cos(\frac{\phi}{2})\cos(\frac{\theta}{2})\cos(\frac{\psi}{2}) + \sin(\frac{\phi}{2})\sin(\frac{\theta}{2})\sin(\frac{\psi}{2}) \\ \sin(\frac{\phi}{2})\cos(\frac{\theta}{2})\cos(\frac{\psi}{2}) - \cos(\frac{\phi}{2})\sin(\frac{\theta}{2})\sin(\frac{\psi}{2}) \\ \cos(\frac{\phi}{2})\sin(\frac{\theta}{2})\cos(\frac{\psi}{2}) + \sin(\frac{\phi}{2})\cos(\frac{\theta}{2})\sin(\frac{\psi}{2}) \\ \cos(\frac{\phi}{2})\cos(\frac{\theta}{2})\sin(\frac{\psi}{2}) - \sin(\frac{\phi}{2})\sin(\frac{\theta}{2})\cos(\frac{\psi}{2}) \end{bmatrix} \end{aligned} \tag{3.11}$$

The kinematic relationship between the different velocities in body or ground reference frames using Euler parameters (q_{0-3}) are given by:

$$\dot{\mathbf{x}} = \begin{bmatrix} \dot{x} \\ \dot{y} \\ \dot{z} \\ \dot{q_0} \\ \dot{q_1} \\ \dot{q_2} \\ \dot{q_3} \end{bmatrix} = \begin{bmatrix} \boldsymbol{\lambda}_1 & 0_{3\times3} \\ 0_{4\times3} & \boldsymbol{\lambda}_2 \end{bmatrix} \begin{bmatrix} u \\ v \\ w \\ p \\ q \\ r \end{bmatrix} \tag{3.12}$$

The orientation matrices $\boldsymbol{\lambda}_1$ and $\boldsymbol{\lambda}_2$ are formulated as follows;

$$\boldsymbol{\lambda}_1 = \begin{bmatrix} 1-2(q_2^2+q_3^2) & 2(q_1q_2-q_3q_0) & 2(q_1q_3+q_2q_0) \\ 2(q_1q_2+q_3q_0) & 1-2(q_1^2+q_3^2) & 2(q_2q_3-q_1q_0) \\ 2(q_1q_3-q_2q_0) & 2(q_2q_3+q_1q_0) & 1-2(q_1^2+q_2^2) \end{bmatrix} \tag{3.13}$$

and

$$\boldsymbol{\lambda}_2 = \frac{1}{2}\begin{bmatrix} -q_1 & -q_2 & -q_3 \\ q_0 & -q_3 & q_2 \\ q_3 & q_0 & -q_1 \\ -q_2 & q_1 & q_0 \end{bmatrix} \tag{3.14}$$

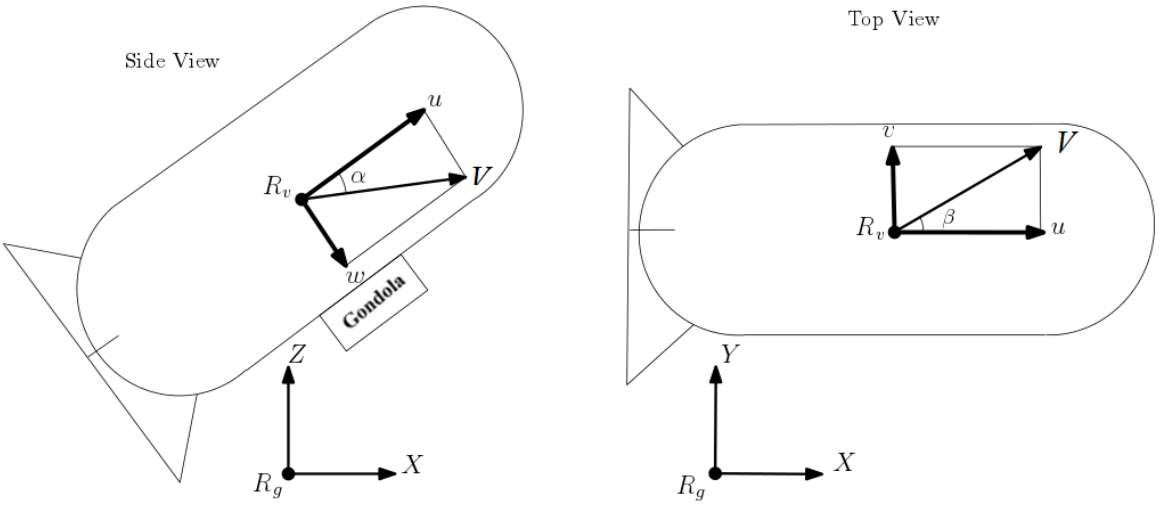

Figure 3.3: Attack α and slideslip β angles of the additional velocity vectors

3.3 Wind disturbances

Wind affects the vehicle state by modifying the air speed around the airship and, as a result, the aerodynamic forces and moments in $\mathbf{A}$. The relative airship speed with respect to the wind in the body reference frame is given by,

$$\dot{\mathbf{x}}_W = \begin{bmatrix} u_W \\ v_W \\ w_W \end{bmatrix} = \begin{bmatrix} u \\ v \\ w \end{bmatrix} - \{\boldsymbol{\lambda}_1\}^{-1}\mathbf{V}_{W_g} \tag{3.15}$$

where $\dot{\mathbf{x}}_W$ is the relative velocity the airship with respect to the wind and $\mathbf{V}_{W_g}$ is the 3x1 longitudinal wind speed vector expressed in the ground reference frame $\mathbf{R_g}$,

$$V_{W_g}(\theta_W, W) = \begin{bmatrix} W\cos(\theta_W) \\ 0 \\ W\sin(\theta_W) \end{bmatrix} \tag{3.16}$$

where W is the wind speed magnitude, and θ_W is the wind direction about the Y axis of $\mathbf{R_g}$. Lateral winds are neglected in 3.16 as the simulations and experimental flight tests assumed zero lateral winds.

3.4 Velocity vector angles

Additional velocity vector angles are illustrated in figure 3.3. These angles are used throughout the modelling:

The attack angle α is,

$$\alpha = \tan^{-1}(\frac{w_W}{u_W}) \tag{3.17}$$

and the sideslip angle β,

$$\beta = \sin^{-1}(\frac{v_W}{V}) \tag{3.18}$$

where V is the magnitude of the vehicle velocity,

$$V = \sqrt{u_W^2 + v_W^2 + w_W^2} \tag{3.19}$$

These velocities and angles will be used to obtain the airship aerodynamic forces and moments.

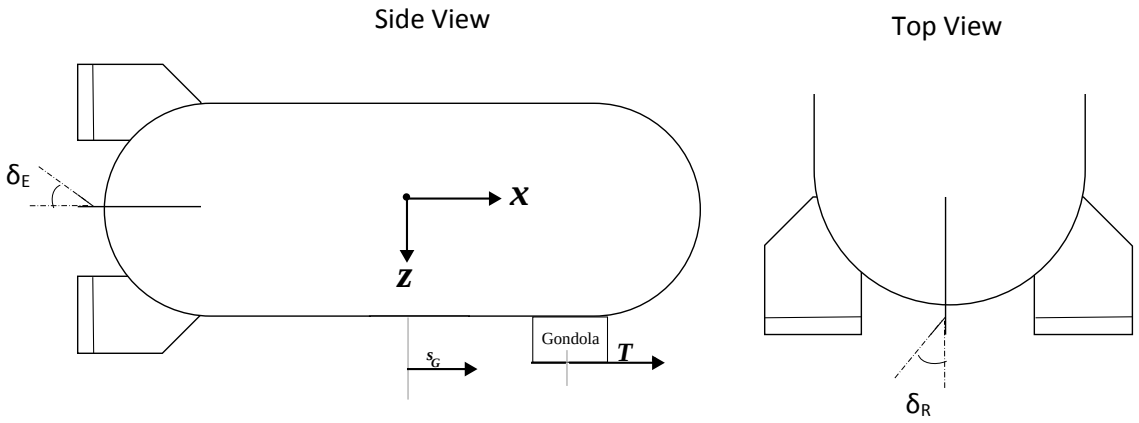

Figure 3.4: Control inputs

3.5 Control inputs

This model has two control surfaces and actuators as seen in Figure 3.4. Elevator δ_E points upward with positive deflection. Rudder δ_R causes positive deflection when it is deflected towards the right side (clockwise around the rudder axes). Positive propeller T increases the forward thrust. Lastly, gondola position s_G is increasing when it is moving forward.

3.6 Equation of Motion

The equation of motion is defined as,

$$\mathbf{M}(\ddot{\mathbf{x}}_\mathbf{v}) = \mathbf{D}(\dot{\mathbf{x}}_\mathbf{v}) + \mathbf{A}(\dot{\mathbf{x}}_\mathbf{W}) + \mathbf{G}(\lambda) + \mathbf{U}_\mathbf{T} \tag{3.20}$$

Where,

M is the 6x6 mass matrix and the added mass due to aerodynamic forces.

D is the 6x1 dynamics vector.

A is the 6x1 aerodynamic vector.

G is the 6x1 gravitational and buoyancy vector.

$\mathbf{U_T}$ is the 6x1 direct forces and moments vector.

3.6.1 Mass Matrix, M

The total mass of the airship can be expressed by the following,

$$m = m_G + m_R + m_E \tag{3.21}$$

where m is the total physical mass of the airship, m_G is the gondola mass, m_E is the envelope mass and m_R is the rail mass. They are shown in Figure 3.1.

Due to the airship symmetry about the XZ plane, the 6 x 6 mass matrix can be simplified by,

$$\mathbf{M} = \begin{bmatrix} \mathbf{M_a} & m\mathbf{d_{CG}^T} \\ m\mathbf{d_{CG}} & \mathbf{J_a} \end{bmatrix} \tag{3.22}$$

where m is the total physical mass of the airship as shown in 3.21, $\mathbf{d_{CG}}$ is a skew symmetric matrix of the CG vector with respect to the CV,

$$\mathbf{d_{CG}} = \begin{bmatrix} 0 & -md_{m,z} & 0 \\ md_{m,z} & 0 & -md_{m,x} \\ 0 & md_{m,x} & 0 \end{bmatrix} \tag{3.23}$$

Since the position of the gondola s_G is controllable, the normal distance from the CV to the CG along x axis is $d_{m,x}$ and along z axis is $d_{m,z}$, and they are given by,

$$d_{m,x} = s_G(\frac{m_G}{m}) \tag{3.24}$$

$$d_{m,z} = \frac{l_R m_R + l_G m_G}{m} \tag{3.25}$$

where l_R is the rail length, l_G is the gondola length, $\mathbf{M_a}$ is composed of the total physical mass and the additional added mass,

$$\mathbf{M_a} = \begin{bmatrix} m_x & 0 & 0 \\ 0 & m_y & 0 \\ 0 & 0 & m_z \end{bmatrix} \tag{3.26}$$

where m_x, m_y and m_z are the composed of the total physical mass and the additional added mass in the x, y and z axes, respectively. $\mathbf{J_a}$ is composed of the inertia of the airship as well as the additional added inertia,

$$\mathbf{J_a} = \begin{bmatrix} J_x & 0 & -J_{xz} \\ 0 & J_y & 0 \\ -J_{xz} & 0 & J_z \end{bmatrix} \tag{3.27}$$

The mass matrix in 3.22 now can be written as,

$$\mathbf{M} = \left[\begin{array}{ccc|ccc} m_x & 0 & 0 & 0 & md_{m,z} & 0 \\ 0 & m_y & 0 & -md_{m,z} & 0 & md_{m,x} \\ 0 & 0 & m_z & 0 & -md_{m,x} & 0 \\ \hline 0 & -md_{m,z} & 0 & J_x & 0 & -J_{xz} \\ md_{m,z} & 0 & -md_{m,x} & 0 & J_y & 0 \\ 0 & md_{m,x} & 0 & -J_{xz} & 0 & J_z \end{array}\right] \tag{3.28}$$

$\mathbf{M_a}$ and $\mathbf{J_a}$ are estimated by these terms,

$$m_x = (1+k_1)m \tag{3.29}$$

$$m_y = m_z = (1+k_2)m \tag{3.30}$$

$$J_x = I_{f,x} + I_{G,x} \tag{3.31}$$

$$J_y = (1+k')I_{f,y} + I_{G,y} \tag{3.32}$$

$$J_z = (1+k')I_{f,z} + I_{G,z} \tag{3.33}$$

$$J_{xz} = I_{f,xz} + I_{G,xz} \tag{3.34}$$

where k_1, k_2 and k' are approximated using the works of Lamp [49] and Munk [50], $I_{f,x}, I_{f,y}, I_{f,xz}$ and $I_{f,z}$ represent the inertias of the fixed components (rail and envelope) and were determined from the computer-aided drafting (CAD) model of the airship, $I_{G,x}, I_{G,y}, I_{G,xz}$ and $I_{G,z}$ represent the inertias of the gondola and they are given by,

$$I_{G,x} = d_{G,z}^2 \tag{3.35}$$

$$I_{G,y} = \sqrt{(s_G^2 + d_{G,z}^2)} \tag{3.36}$$

$$I_{G,z} = s_G^2 \tag{3.37}$$

$$I_{G,xz} = -s_G d_{G,z} \tag{3.38}$$

where $d_{G,z}$ is the normal distance from the CV to the gondola CG along z axis. In table 3.1, there are the geometric and physical properties of the simulated airship.

Table 3.1: Airship physical properties

Symbol	Description	Value
m_E	Envelope mass	220 g
m_R	Rail mass	19 g
m_G	Gondola mass	121 g
k_1	Lamb's inertia ratio about x	0.1069
k_2	Lamb's inertia ratio about y or z	0.8239
k'	Lamb's inertia ratio about y or z	0.5155
V	Airship volume	0.311 m^3
L	Airship length	1.75 m
D	Airship diameter	0.5 m
$d_{G,z}$	CV to gondola CG distance along z	0.27 m
$d_{G,x}$	CV to fin center distance along x	0.8 m
$d_{f,z}$	CV to fin center distance along z	0.27 m

3.6.2 Dynamic vector, $\mathbf{D}(\dot{\mathbf{x}}_\mathbf{v})$

The dynamic vector contains the Coriolis and centrifugal terms of the dynamic model associated with inertial linear velocity (u, v, w) and angular velocity (p, q, r) and can be expressed as:

$$\mathbf{D}(\dot{\mathbf{x}}_\mathbf{v}) = [D_X \; D_Y \; D_Z \; D_L \; D_M \; D_N]^{\mathrm{T}} \tag{3.39}$$

where,

$$D_x = -m_z wq + m_y rv + m[d_{m,x}(q^2 + r^2) - d_{m,z}rp] \tag{3.40}$$

$$D_y = -m_x ur + m_z pw + m[d_{m,x}pq + d_{m,z}rq] \tag{3.41}$$

$$D_z = -m_y vp + m_x qu - m[d_{m,z}(q^2 + p^2) - d_{m,x}rp] \tag{3.42}$$

$$D_\phi = -(J_z - J_y)rq - J_{xz}pq + md_{m,z}(ur - pw) \tag{3.43}$$

$$D_\theta = -(J_x - J_z)pr - J_{xz}(r^2 - p^2) + m[d_{m,x}(vp - qu) - d_{m,z}(wq - rv)] \tag{3.44}$$

$$D_\psi = -(J_y - J_x)qp + J_{xz}qr - md_{m,x}(ur - pw) \tag{3.45}$$

3.6.3 Aerodynamic vector, **A**

The aerodynamics vector **A** in this thesis is derived by Recoskie [35] in his research which is derived based on the work of both Jones and Mueller [21, 51] with additional rotational dampening added.

The aerodynamic vector is given by,

$$\mathbf{A}(\dot{\mathbf{x}}_{\mathbf{w}}) = [A_x \; A_y \; A_z \; A_\phi \; A_\theta \; A_\psi]^{\mathrm{T}} \tag{3.46}$$

where;

$$A_x = P[C_{X1}cos(\alpha)^2 cos(\beta)^2 + C_{X2}(sin(2\alpha)sin(\alpha/2) + sin(2\beta)sin(\beta/2))] \tag{3.47}$$

$$A_y = P(C_{Y1}cos(\beta/2)sin(2\beta) + C_{Y2}sin(2\beta) + C_{Y3}sin(\beta)sin(|\beta|) + C_{Y4}(2\delta_R)) \tag{3.48}$$

$$A_z = P(C_{Z1}cos(\alpha/2)sin(2\alpha) + C_{Z2}sin(2\alpha) + C_{Z3}sin(\alpha)sin(|\alpha|) + C_{Z4}(2\delta_E)) \tag{3.49}$$

$$A_\phi = PC_{\phi 1}sin(\beta)sin(|\beta|) + \rho_a C_{\phi 3} p|p|/2 + \rho_a C_{\phi 3} r|r|/2 \tag{3.50}$$

$$A_\theta = P(C_{\theta 1}cos(\alpha/2)sin(2\alpha) + C_{\theta 2}sin(2\alpha) + C_{\theta 3}sin(\alpha)sin(|\alpha|) \tag{3.51}$$

$$+ C_{\theta 4}(2\delta_E)) + \rho_a C_{\theta 5} q|q|/2 \tag{3.52}$$

$$A_\psi = P(C_{\psi 1}cos(\beta/2)sin(2\beta) + C_{\psi 2}sin(2\beta) + C_{\psi 3}sin(\beta)sin(|\beta|) \tag{3.53}$$

$$+ C_{\psi 4}(2\delta_R)) + \rho_a C_{\psi 5} r|r|/2 \tag{3.54}$$

where $P = 1/2\rho_a V^2$ is the steady state dynamic pressure, ρ_a is the air density.

The coefficients of the aerodynamic terms are given by:

$$
\begin{aligned}
C_{X1} &= -[C_{Dho}S_h + C_{Dfo}S_f + C_{DGo}S_G] && (3.55)\\
C_{X2} &= -C_{Y1} = -C_{Z1} = (k_2 - k_1)\eta_k I_1 S_h && (3.56)\\
C_{Y2} &= C_{Z2} = -\frac{1}{2}\left(\frac{\delta C_L}{\delta \alpha}\right)_f S_f \eta_f && (3.57)\\
C_{Y3} &= -[C_{Dch}J_1 S_h + C_{Dcf}S_f + C_{DcG}S_G] && (3.58)\\
C_{Y4} &= C_{Z4} = -\frac{1}{2}\left(\frac{\delta C_L}{\delta \alpha}\right)_l S_f \eta_f && (3.59)\\
C_{Z3} &= -[C_{Dch}J_1 S_h + C_{Dcf}S_f] && (3.60)\\
C_{\phi 1} &= C_{DcG}S_G d_{G,z} && (3.61)\\
C_{\phi 2} &= -2C_{Dcf}S_f d_{f,z}^3 && (3.62)\\
C_{\phi 3} &= -C_{DcG}S_G d_{G,z} D^2 && (3.63)\\
C_{\theta 1} &= -C_{\psi 1} = (k_2 - k_1)\eta_k I_3 S_h L && (3.64)\\
C_{\theta 2} &= -C_{\psi 2} = -\frac{1}{2}\left(\frac{\delta C_L}{\delta \alpha}\right)_f S_f \epsilon_f d_{f,x} && (3.65)\\
C_{\theta 3} &= -[C_{Dch}J_2 S_h L + C_{Dcf}S_f d_{f,x}] && (3.66)\\
C_{\psi 3} &= C_{Dch}J_2 S_h L + C_{Dcf}S_f d_{f,x} + C_{DcG}S_G s && (3.67)\\
C_{\theta 4} &= -C_{\psi 4} = -\frac{1}{2}\left(\frac{\delta C_L}{\delta \delta_{E,R}}\right)_l S_f \epsilon_f d_{f,x} && (3.68)\\
C_{\theta 5} &= -C_{Dcf}S_f d_{f,x}^3 && (3.69)\\
C_{\psi 5} &= -[C_{Dcf}S_f d_{f,x}^3 - C_{DcG}S_G s_G^3] && (3.70)
\end{aligned}
$$

3.6.4 gravitational and buoyancy vector, $\mathbf{G}(\lambda)$

The gravitational and buoyancy vector is given by,

$$\mathbf{G}(\boldsymbol{\lambda}) = \begin{bmatrix} m\mathbf{g} \\ m\mathbf{d_{CG}}\mathbf{g} \end{bmatrix} - \begin{bmatrix} \rho_a U\mathbf{g} \\ \rho_a U\mathbf{d_{CG}}\mathbf{g} \end{bmatrix} \tag{3.71}$$

where $\mathbf{d_{CG}}$ is defined in 3.23, $\mathbf{g} = \boldsymbol{\lambda}^T[0\ 0\ g]^T$ is the gravitational vector expressed in the body frame using the directional cosine matrix $\boldsymbol{\lambda}$ which is defined in 3.5 and 3.13, g is the standard acceleration due to gravity, and U is the volume of the helium envelope. The gravitational and buoyancy vector becomes [35],

$$\mathbf{G}(\boldsymbol{\lambda}) = [G_x\ G_y\ G_z\ G_\phi\ G_\theta\ G_\psi]^T \tag{3.72}$$

Table 3.2: Simulated airship aerodynamic properties

Symbol	Description	Value
C_{Dho}	Hull zero-incidence drag coefficient [52]	0.024
C_{Dfo}	Fin zero-incidence drag coefficient [52]	0.003
C_{DGo}	Gondola zero-incidence drag coefficient [51]	0.01
C_{Dch}	Hull cross-flow drag coefficient [52]	0.32
C_{Dcf}	Fin cross-flow drag coefficient [53]	2
C_{DcG}	Gondola cross-flow drag coefficient [51]	.25
$(\frac{\delta C_L}{\delta \alpha})_f$	Derivative of fin lift coefficient with respect to angle of attack [53]	5.73
$(\frac{\delta C_L}{\delta \delta_{E,R}})_f$	Derivative of fin lift coefficient with respect to fin angle [53]	1.24
S_h	Hull reference area $V^{(2/3)}$	0.46 m^2
S_f	Fin reference area [30]	0.172 m^2
S_G	Gondola reference area [30]	0.0025 m^2
n_f	Fin efficiency factor [21]	0.4
n_k	Hull efficiency factor [21]	1.05
I_1	Hull integrals [51]	0
I_3		-1.0839
J_1		1.7897
J_2		0.6809

where,

$$G_x = (m - \rho_a U) g_1 \tag{3.73}$$

$$G_y = (m - \rho_a U) g_2 \tag{3.74}$$

$$G_z = (m - \rho_a U) g_3 \tag{3.75}$$

$$G_\phi = -m d_{mz} g_2 \tag{3.76}$$

$$G_\theta = m(d_{mz} g_1 - d_{mx} g_3) \tag{3.77}$$

$$G_\psi = m d_{mx} g_2 \tag{3.78}$$

3.6.5 Direct forces and moments vector, $\mathbf{U_T}$

The sum of all actuator forces as the apply in the body frame is,

$$\mathbf{U_T} = \begin{bmatrix} T_R + T_L \\ 0 \\ 0 \\ 0 \\ (T_R + T_L)d_{G,z} \\ (T_L - T_R)d_{G,y} \end{bmatrix} \tag{3.79}$$

where T_R and T_L are the right and left propeller thrust, respectively, and $d_{G,z}$ and $d_{G,y}$ are the normal distances from the right and left propeller centers to the $x-z$ plane as shown in Figure 3.2.

3.7 Six-degree-of-freedom simulation model with wind disturbance

The purpose of the simulations is to observe the behavior of the model under disturbances. The sex DOF simulation model for the airship model was implemented in Matlab/Simulink. Figure 3.5 shows the main components of the model including the wind disturbances and the airship dynamic model.

3.7.1 Open-loop simulation

The open-loop simulation in Figure 3.6 shows of the linear and angular displacements, x y z ϕ θ and ψ in the ground reference frame $\mathbf{R_g}$, and the linear and angular velocities, u v w p q and r in the body reference frame $\mathbf{R_v}$. The simulation was run for 300 seconds. The initial conditions include the gondola position $s_G = 0$, all the airship linear and angular displacements and velocities are zero except the altitude h is 180 m which correspond to the neutrally buoyant altitude of the test area. Through out the simulation, the elevator δ_E and the rudder δ_R deflections are zero and the thrust input is $T_L = T_R = 0.1$N.

As the motors are under the center of gravity of the airship, the thrust produces a moment that increases the pitch θ while the airship accelerates. This phenomenon can be seen during the first 20 seconds in the simulation. Moreover, the altitude z

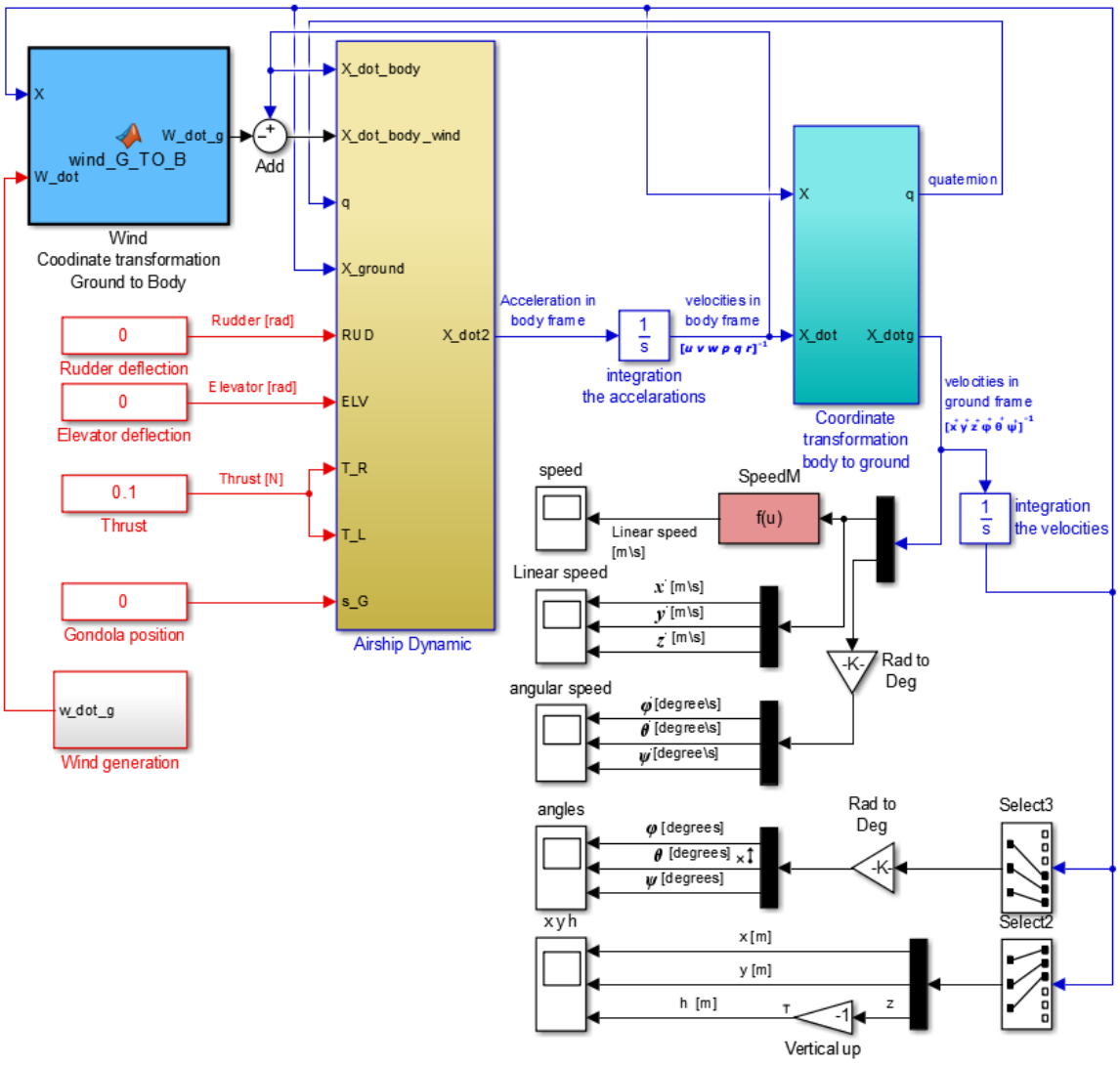

Figure 3.5: Six DOF implemented Simulink model

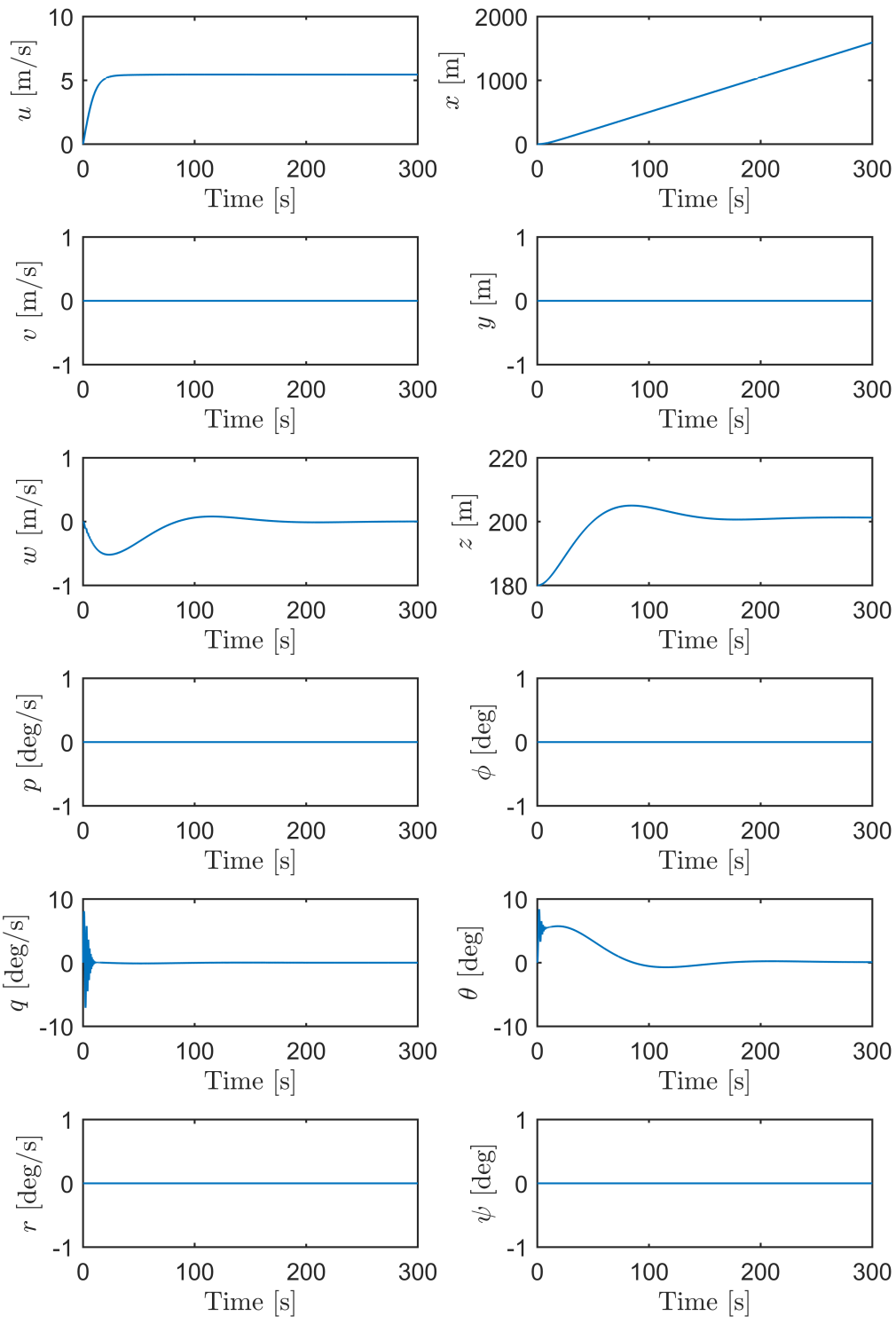

Figure 3.6: Open-loop simulation of the linear and angular displacements, x y z ϕ θ and ψ in the ground reference frame $\mathbf{R_g}$, and the linear and angular velocities, u v w p q and r in the body reference frame $\mathbf{R_v}$.

increased from 180 m to 205 m then reached a steady state altitude at 202 m as a result of the positive degree of pitch angle θ at the beginning of the simulation.

3.7.2 Open-loop simulation with wind disturbances

The simulation will show the effects of the thrust and the wind on the airship pitch angle θ and altitude h. The initial conditions include the gondola position $s_G = 0$, all the airship linear and angular displacements and velocities are zero except the altitude h is 180 m as this represents the altitude of the test area. Through out the simulation, the elevator δ_E and the rudder δ_R deflections are fixed to zero.

The simulation was run for 200 seconds for four times in different cases of wind and thrust as seen in Figure 3.7. Figure 3.7-a shows the results on the airship altitude and traveling distance x in $\mathbf{R_g}$. Figure 3.7-b illustrates the time transition of the pitch angle. Lastly, figure 3.7-c illustrates the first 20 seconds of figure 3.7-b. Wind direction and plots legend are illustrated at the bottom of the figure 3.7.

First case run with wind speed $W = 0$ and both thruster $T_R = T_L = 0$ N throughout the simulations. The plots show no change in the airship altitude, traveled distance, and pitch angle. As expected, the airship is in the equilibrium position, and there are no changes in altitude and pitch angle with no distance traveled. These results illustrate that any changes in the altitude or the pitch angle caused by wind disturbances or thrust.

The second case introduces a wind speed $W = 1$ m/s and direction $\theta_W = -45^o$ in the $\mathbf{R_g}$ and both thruster $T_R = T_L = 0$ N throughout the simulations. As illustrated in figure 3.7-a, solid line, the wind pushes the airship down and forward as expected from the wind direction. Moreover, the wind generated oscillation for about 80 seconds as illustrated by the solid line in Figure 3.7-b and 3.7-c. The pitch angle first reached 77^o upwards and then -24^o downwards as the initial wind speed went from zero to 1 m/s. The pitch angle reached steady state value of around 23^o after 160 seconds without oscillation.

The third case shows the results with a wind speed of $W = 0$ and both thruster at $T_R = T_L = 0.10$ N. The dash-dot line in Figure 3.7-a shows that the airship traveled

for 1593 m in the x direction. The dash-dot line illustrated in Figure 3.7-b and 3.7-c shows light oscillations between 8° and 3° for about 8 seconds then the vehicle reaches steady state at approximately 80 second.

In the fourth case, a wind speed of $W = 1$ m/s direction $\theta_W = -45°$ is introduced. The dash line in Figure 3.7-a shows that the airship traveled for 1065 m in the x direction. The trajectory shows no oscillation but the pitch angle reach 74° in two second then decreased slowly and study state around 8°.

The open-loop model was then tested with a random wind speed magnitude W = 0.50 to 2.00 m/s with a maximum speed rate change 0.25 m/s^2. Two Simulink blocks are used to generate the desired random wind, Uniform Random Number and Rate Limiter. Figure 3.8 illustrates the pitch angle θ in the case of the constant wind speed $W = 1$ m/s and random wind speed. As seen in the Figure 3.8 that the pitch angle quantifies the difference between random and constant wind. The large pitch angle at the start of the simulation was a result of the transition between no wind as t = 0 seconds and the applied wind thereafter.

The model was simulated with different wind direction, $\theta_W = +45°$, and same wind speed, $W = 1$ m/s, as shown in Figure 3.9. As expected from the wind direction, the wind pushes the airship up and forward at the zero thrust input case, solid line. The dashed line illustrates the case of wind speed $W = 1$ m/s and both thruster $T_R = T_L = 0.10$ N throughout the simulations.

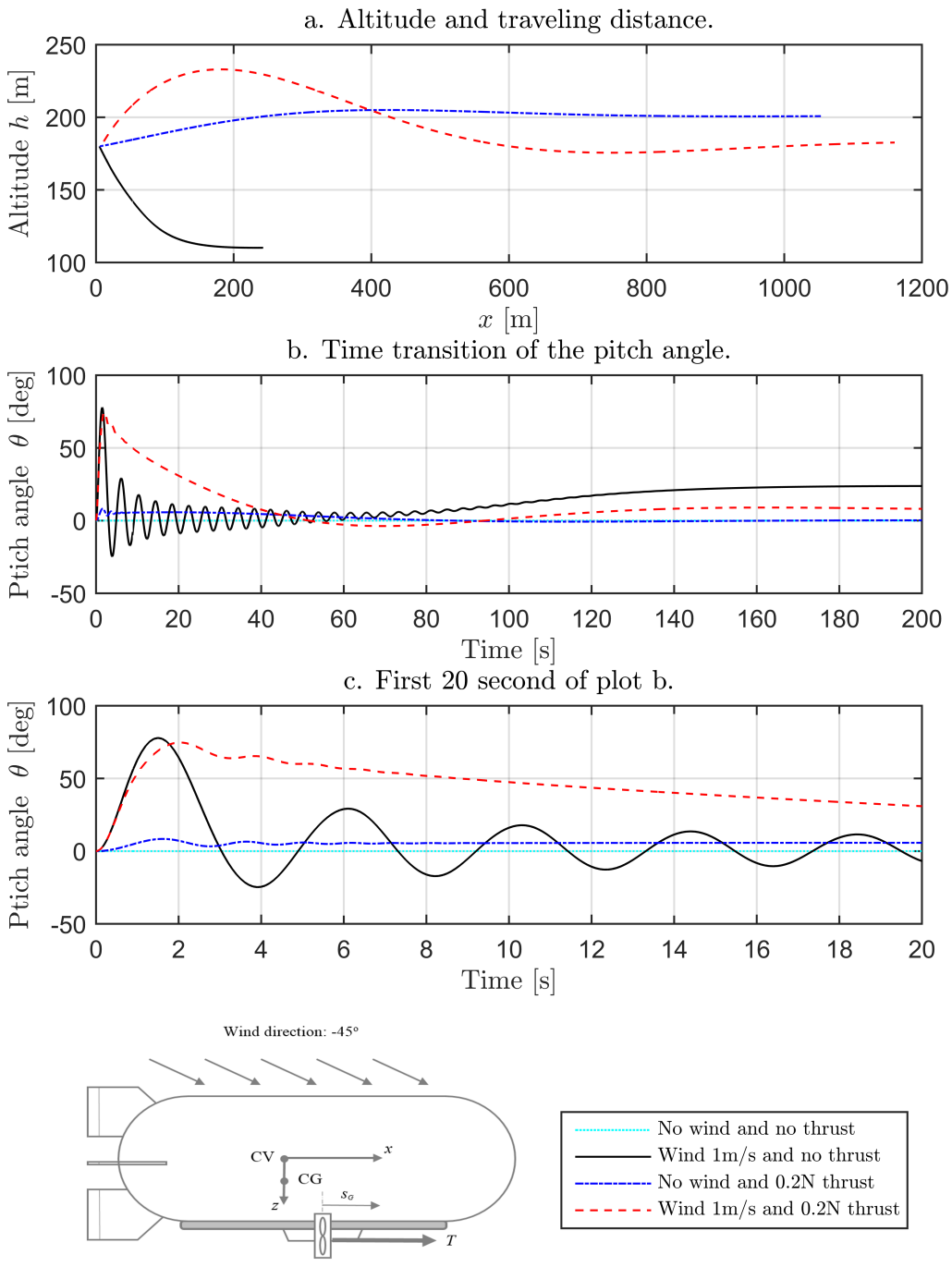

Figure 3.7: Open-loop plots in different cases of wind and thrust.

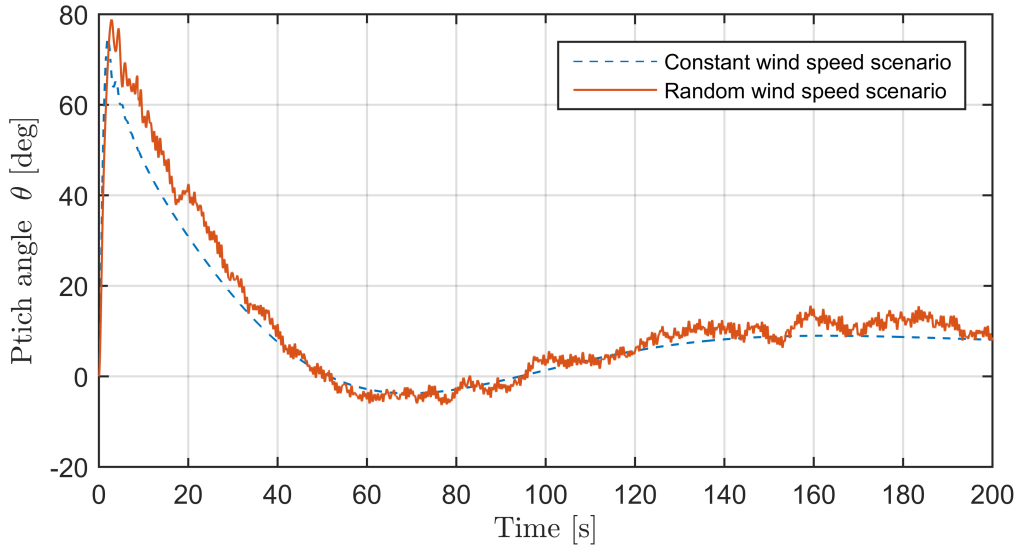

Figure 3.8: Open-loop plots of the pitch angle in the case of constant wind speed 1 m/s and random speed 0.5 - 2 m/s.

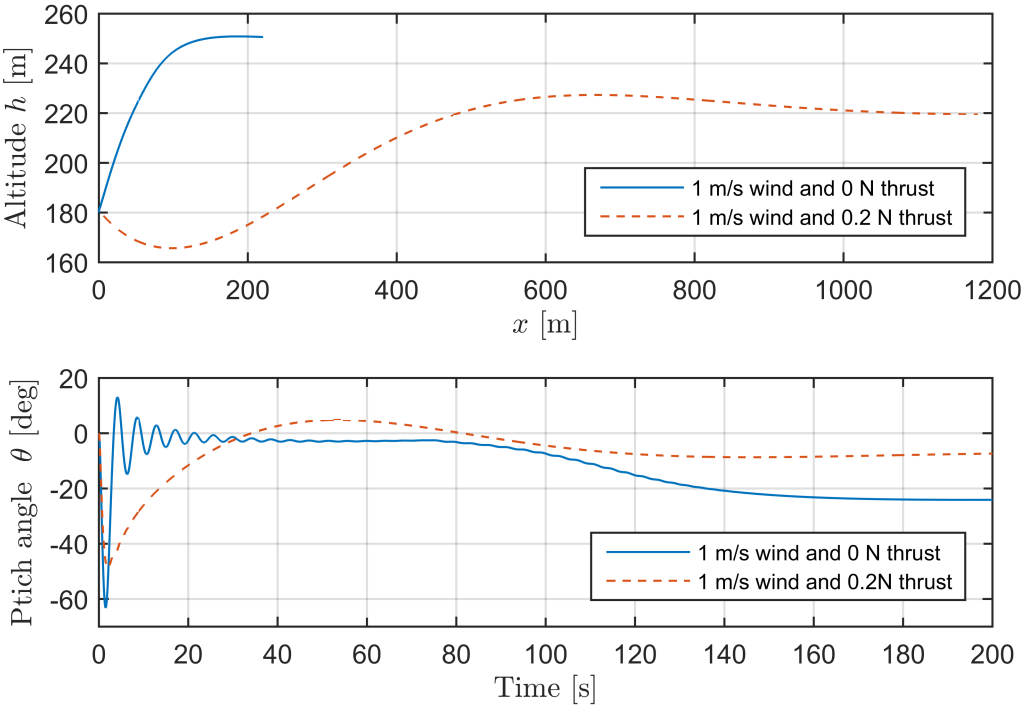

Figure 3.9: Open-loop plots in case of $+45^{o}$ wind.

Chapter 4

Airship control

4.1 Introduction

The purpose of this chapter is to illustrate that the pitch angle and altitude can be controlled in closed-loop. The equations of motion developed in Chapter 3 were trimmed and linearized at an operation point to obtain two transfer functions between the gondola position s_G and the altitude h, and between the gondola position s_G the pitch angle θ. The PID controllers for the airship pitch angle and altitude were then designed from the transfer functions. Closed-loop simulations were performed with different reference inputs for the controller with and without wind disturbance in continuous time. Pitch control was then simulated in discrete time to respect the capabilities of the experimental platform.

4.2 Airship model linearizion

The complete non-linear model of the airship consists of six equations of motion $\mathbf{F}$ which consist of the state variables $\mathbf{X} = [u\ v\ w\ p\ q\ r\ x\ y\ z\ \phi\ \theta\ \psi]^{\mathrm{T}}$ that includes the airship linear and angular velocities and the airship Euler angles and displacements, and the input $\mathbf{U} = [s_G\ T]^{\mathrm{T}}$ that includes the gondola position and the thrust,

$$\dot{\mathbf{X}} = \mathbf{F}(\mathbf{X}, \mathbf{U}) \tag{4.1}$$

To derive the linear dynamics model, an equilibrium state or a trim point $\mathbf{X_e}$ is first required. The trim point is when the dynamic system is in a steady state or mathematically where the system's state derivatives equal zero. For a straight and level flight, the trim point of the airship can be obtained around a constant axial velocity and altitude.

The non-linear equations are linearized around the equilibrium state $\mathbf{X_e}$ by calculating the Jacobian of the non-linear equation with regards to the states $\mathbf{X}$,

$$\mathbf{A} = \frac{\partial \mathbf{F}}{\partial \mathbf{X}} \mid_{\mathbf{x_e}} \tag{4.2}$$

and with regards to the input $\mathbf{U}$,

$$\mathbf{B} = \frac{\partial \mathbf{F}}{\partial \mathbf{U}} \mid_{\mathbf{x_e}} \tag{4.3}$$

The linearized model for small perturbations around the trim point $\mathbf{X_e}$ is given by,

$$\dot{\mathbf{X}} = \mathbf{A}\ \Delta\mathbf{X} + \mathbf{B}\ \Delta\mathbf{U} \tag{4.4}$$

Numerical trim point and linearization are achieved in the next section by using the Linear Analysis Tool (LAT) from Matlab.

4.2.1 Trim point

The six DOF model was trimmed For straight and level flight at an altitude of 180 m and thrust input $T_R = T_L = 0.1$ N. The trim point is as follow,

$$\begin{aligned} \mathbf{X_e} &= [u_o\ v_o\ w_o \quad p_o\ q_o\ r_o \quad x_o\ y_o\ z_o \quad \phi_o\ \theta_o\ \psi_o]^{\mathrm{T}} \\ &\approx [5.44\ 0\ 0 \quad 0\ \ 0\ \ 0 \quad 0 \quad 0\ 180 \quad 0\ \ 0\ \ 0]^{\mathrm{T}} \end{aligned} \tag{4.5}$$

where the linear axial speed $u_o = 5.44$ m/s is the expected speed at the input thrust. The input gondola position at the trim point was $s_G = 0.045$ m which was obtained by sitting s_G as a variable and the LAT will find the value of the gondola position that gives the equilibrium $\mathbf{X_e}$.

Figure 4.1 shows the open-loop simulation at the operating point $\mathbf{X_e}$ for the pitch angle θ and the altitude h with input $\mathbf{U}$ is 0.045 m for the gondola position s_G and $T_R = T_L = 0.1$ N for the thrust input. The simulation shows that the model was successfully trimmed.

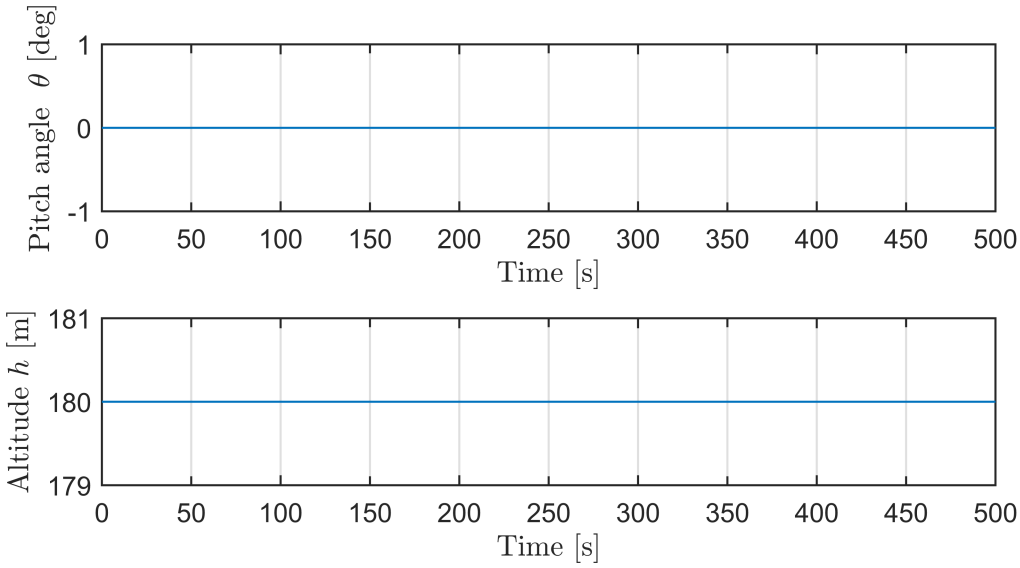

Figure 4.1: The open-loop simulation at the operating point for the pitch angle θ and the altitude with input $\mathbf{U}$ is 0.045 m for the gondola position s_G and $T_R = T_L = 0.1$ N for the thrust input.

4.2.2 Longitudinal flight

The trim point was then used to linearized the model with the gondola position s_G as the input $\mathbf{U}$ and the airship pitch θ and altitude h as the output $\mathbf{y}$. The longitudinal dynamic can be describe by the forward velocity u, the vertical velocity w, the pitch rate q and the pitch angle θ. Therefore the state vector is given by,

$$\mathbf{X}_{long} = [\ u\ w\ q\ \theta\ ]^{\mathrm{T}} \tag{4.6}$$

The longitudinal linear equation is written in a standard state space form as follows,

$$\dot{\mathbf{X}}_{long} = \mathbf{A}\mathbf{X}_{long} + \mathbf{B}\mathbf{U} \tag{4.7}$$

$$\mathbf{y} = \mathbf{C}\mathbf{X}_{long} + \mathbf{D}\mathbf{U} \tag{4.8}$$

The numerical values of $\mathbf{A}$, $\mathbf{B}$, $\mathbf{C}$ and $\mathbf{D}$ matrices of the state space were obtained from the Matlab/LAT around the operating point $\mathbf{X_e}$, and are given as follows,

$$\mathbf{A} = \begin{bmatrix} -0.1882 & 3.558 & 0.008107 & 0.2546 \\ 0.0004219 & -2.206 & 3.302 & -0.02256 \\ 0.05061 & -37.82 & -0.08617 & -2.706 \\ 0 & 0 & 1 & 0 \end{bmatrix} \tag{4.9}$$

$$\mathbf{B} = \begin{bmatrix} 0.8195 \\ -0.07261 \\ -8.711 \\ 0 \end{bmatrix} \tag{4.10}$$

$$\mathbf{C} = \begin{bmatrix} 0 & 0 & 0 & 1 \\ 0 & 0 & 0 & 0 \end{bmatrix} \tag{4.11}$$

$$\mathbf{D} = \begin{bmatrix} 0 \\ 0 \end{bmatrix} \tag{4.12}$$

4.2.3 Stability and model analysis

The stability of the airship can be characterized by the eigenvalues and the eigenvectors of the matrix **A**. The real eigenvalues represent non oscillatory modes, and the complex conjugates as $\lambda_{1,2} = \sigma \pm jw_o$ represent oscillatory modes. The longitudinal model has two real eigenvalues, $\lambda_1 = -0.1834$ and $\lambda_2 = -0.0401$, and one complex conjugate, $\lambda_{3,4} = -1.1284 \pm 11.2438i$. The airship is stable as the real parts of the eigenvalues are negative, and they are illustrated in the pole-zero map in Figure 4.2.

The eigenvalues and their eigenvectors are shown in table 4.1. The first eigenvalue is called *surge mode* since it shows the behavior of the axial velocity u. The second eigenvalue is called *heave mode* since it indicates the behavior of the vertical velocity w. The complex eigenvalues show the *longitudinal pendulum mode*.

The state equation is solved to obtain the transfer function. Because the solution involves algebraic manipulation, it is necessary first to obtain the Laplace transform of the state equation with initial conditions, the trim point $\mathbf{X_e}$, as follows,

$$s\mathbf{X}(s) = \mathbf{A}\mathbf{X}(s) + \mathbf{B}\mathbf{U}(s) \tag{4.13}$$

$$s\mathbf{y}(s) = \mathbf{C}\mathbf{X}(s) + \mathbf{D}\mathbf{U}(s) \tag{4.14}$$

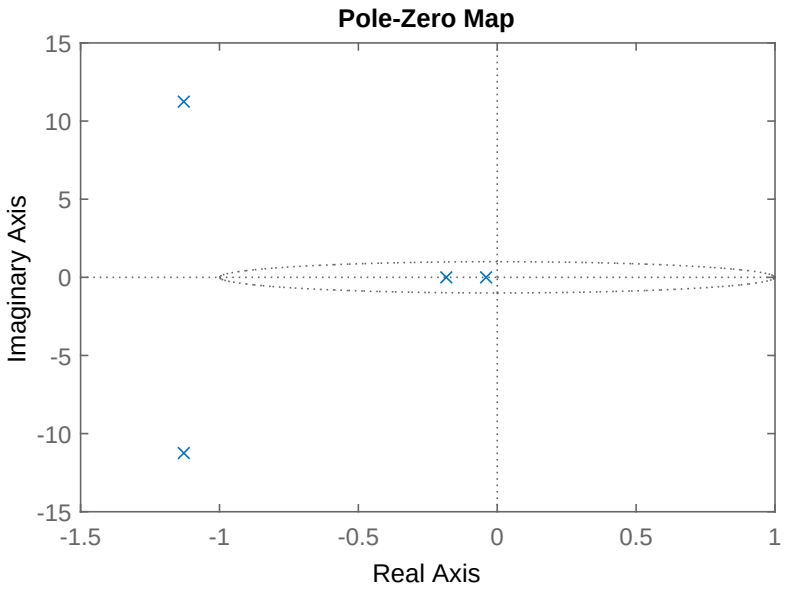

Figure 4.2: Poles and zeros of the longitudinal model.

The solution of the state equation is given by,

$$\mathbf{X}(s) = (s\mathbf{I} - \mathbf{A})^{-1}\mathbf{B}\mathbf{U}(s) = \mathbf{H}(s)\mathbf{U}(s) \tag{4.15}$$

where $\mathbf{I}$ is a unit matrix and $\mathbf{H}(s)$ is the transfer function.

Two single-input single-output (SISO) transfer functions from the input (gondola position, s_G (m)) to the output (pitch angle, θ (rad)) and (airship altitude, h (m)) are given by,

$$\mathbf{H}(s) = \frac{\theta(s)}{s_G(s)} = \frac{-8.711s^2 - 18.07s - 3.021}{s^4 + 2.48s^3 + 128.2s^2 + 28.56s + 0.9385} \quad \text{(rad/m)} \tag{4.16}$$

$$\mathbf{H}(s) = \frac{h(s)}{s_G(s)} = \frac{0.07261s^3 - 18.63s^2 - 93.08s - 16.44}{s^4 + 2.48s^3 + 128.2s^2 + 28.56s + 0.9385} \quad \text{(m/m)} \tag{4.17}$$

4.3 PID Controller for pitch angle and altitude of the airship

The PID controller is added to the model of the airship in the Simulink environment. The controller input is gondola displacement s_G. A rate limiter and saturation were

Table 4.1: Eigenvalues and eigenvectors of airship.

	Eigenvalues		
	-0.1834	-0.0401	$-1.1284 \pm 11.2438i$
u	$1.0000\angle 0°$	$0.0047\angle 180°$	$0.0885 \angle \pm -84.2689°$
w	$0.0009\angle 180°$	$1.0000\angle 0°$	$0.9269\angle \pm 130.4°$
q	$0.0715\angle 180°$	$0.0017\angle 0°$	$0.2923\angle \pm 95.5088°$
θ	$0.0401\angle 180°$	$0.0009\angle 0°$	$1.0000\angle \pm 180°$

added to the output of the PID controller as to respect the capabilities of the experimental platform. The rate limiter is 0.5 m/s, and the saturation is -0.45 m to 0.5 m.

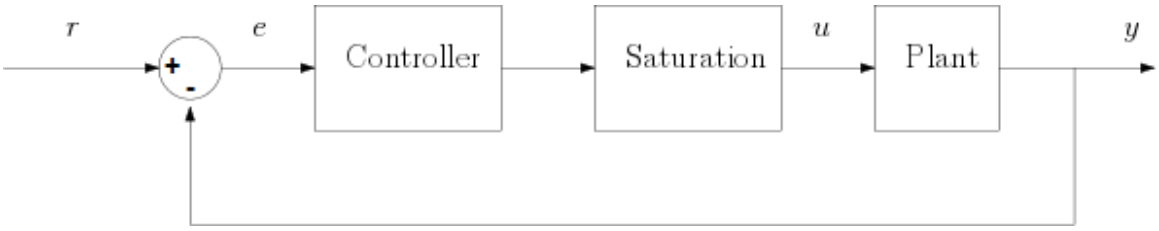

Figure 4.3: PID controller diagram

Figure 4.3 shows the general diagram of the airship model with a PID controller. The output of a PID controller is equal to the control input to the airship model. In the time-domain, the controller output can be given by,

$$u(t) = K_p e(t) + K_i \int e(t)dt + K_d \frac{de}{dt} \tag{4.18}$$

with its Laplace transform,

$$C(s) = K_p + K_i \frac{1}{s} + K_d s \tag{4.19}$$

For practical implementation, it is quite common to modify the derivative term to an low pass filter (LPF) to avoid taking derivatives of high-frequency noise that can be present in the controller input [54],

$$C(s) = K_p + K_i \frac{1}{s} + K_d \frac{Ns}{s+N} \tag{4.20}$$

Table 4.2: Controller Parameters for Pitch Angle Control

Controller Parameters	
K_p	-0.042
K_i	-0.0031
K_d	0.053
N	0.79

where K_p, K_i and K_d are the controller parameters, and they are defined in table 4.2 for pitch control and 4.3 for altitude control, N is the low pass filter coefficient, $u(t)$ is the controller output, $e(t)$ is the error between the desired and plant output and r is the desired input.

Tuning the PID is the method of finding the values of proportional K_p, integral K_i and derivative K_d gains of a PID controller. The controller can be tuned manually by modifying the controller gains and test them in the simulation. This method generally requires experience in tuning. PID tuner is available in PID controller block which is added to the implemented six DOF model of the airship model in Matlab/Simulink. The PID tuner uses a frequency-based design algorithm. The gains are adjusted based on robustness and speed goals that can be set in the tuner as shown in Figure 4.4.

The tuner is used to tune first the controller to achieve desired performance and meet design requirements. The system that is used to tune the controller is the transfer function (4.16) and (4.17) of the linear equations. The controllers were tuned based on a linearized model. To ensure the system behavior in the sex DOF nonlinear model is stable, the controllers are tested in the closed-loop simulation. The gains are tuned in order to make an extra adjustment by trial and error method. The final controllers parameters are in table 4.2 for pitch control and table 4.3 for altitude control. The gains are negative because the pitch angle θ and altitude h decreases when the gondola position s_G increases.

Table 4.3: Controller Parameters for Altitude Control

Controller Parameters	
K_p	-0.06
K_i	-0.0001
K_d	-0.40
N	0.73

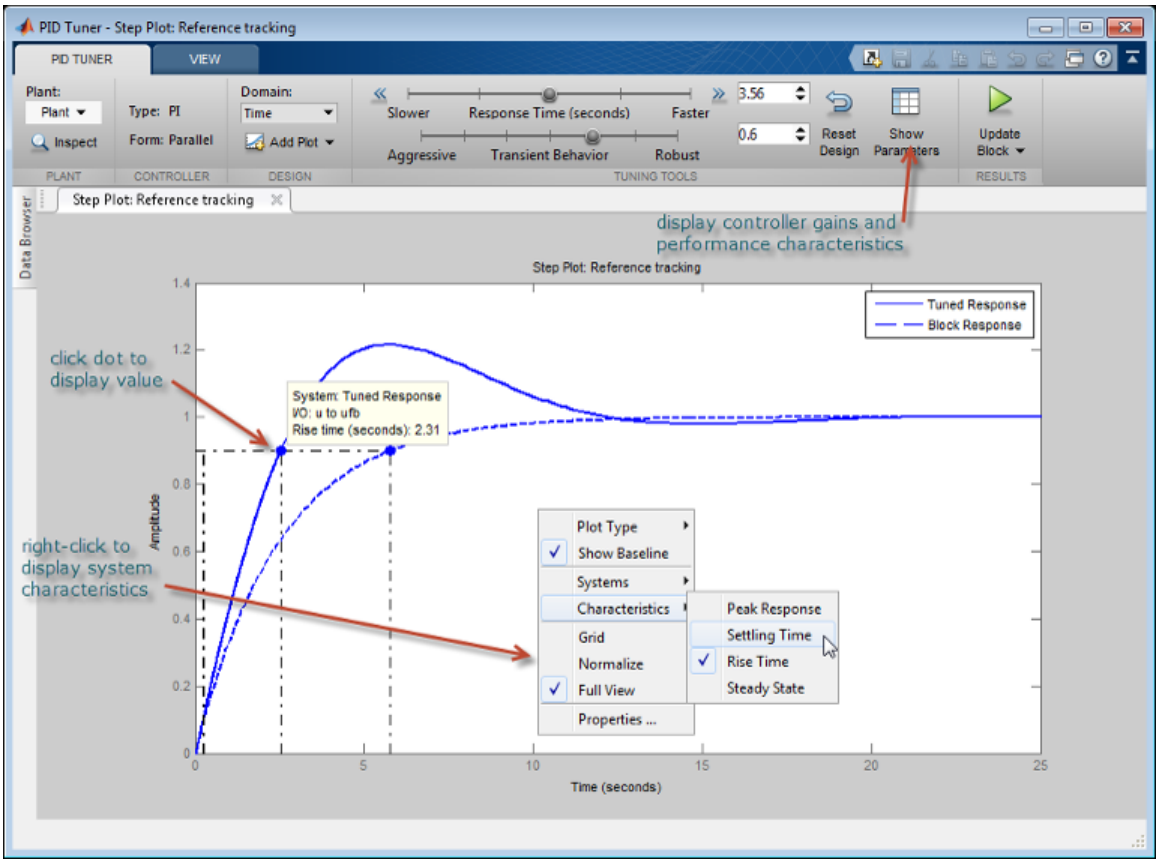

Figure 4.4: PID Tuner.

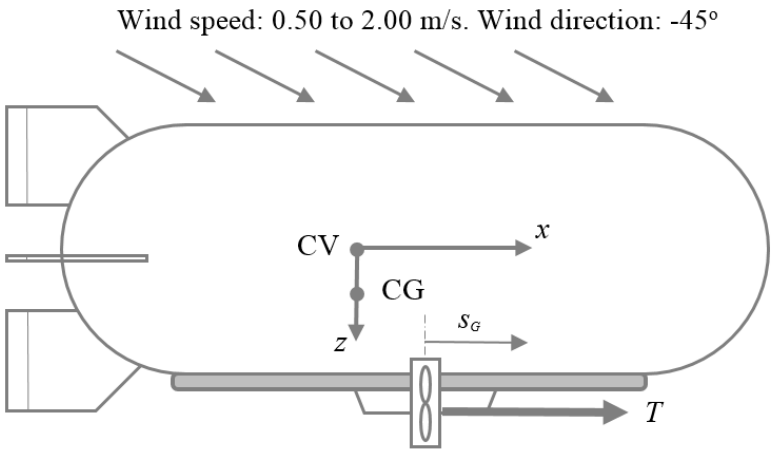

Figure 4.5: Airship diagram and wind direction.

4.4 Simulation of the airship pitch and altitude control

Similar to the open-loop trajectories generated in the previous section, the thrusters were fixed to $T_R = T_L = 0.1$ N, the rudder angle δ_R and the elevator angle δ_L were set to zero throughout the simulations. The initial conditions of the system include a gondola position of $s_G = 0$ m, an altitude of 180 m and a linear speed u of 5.4 m/s which is the trim speed at the input thrust. The maximum speed of the gondola $\dot{s}_G$ is 0.5 m/s, and the saturation is -0.45 m to 0.5 m. Firstly, the airship was tested in an undisturbed environment with two different reference inputs: sinusoidal and wave pulse for pitch and altitude control. Then, the airship was tested with the same reference inputs while under the influence of wind. The wind characteristics include wind speed magnitude W random between 0.50 to 2.00 m/s with maximum speed rate change 0.25 m/s^2 and wind direction θ_W of -45° as illustrated in Figure 4.5.

4.4.1 Simulation results of the pitch angle controller

The first reference pitch input is a sinusoidal path with a frequency of 0.10 rad/sec, an amplitude of 20° and bias of 0 which is a constant value that is added to the input. Figure 4.6 illustrates the plots of the simulation in the case of no wind disturbance, and figure 4.7 illustrates the plots in the case of wind disturbance. Plot 4.6-a and 4.7-a illustrate the pitch angle tracking, and the controller output is shown in plot

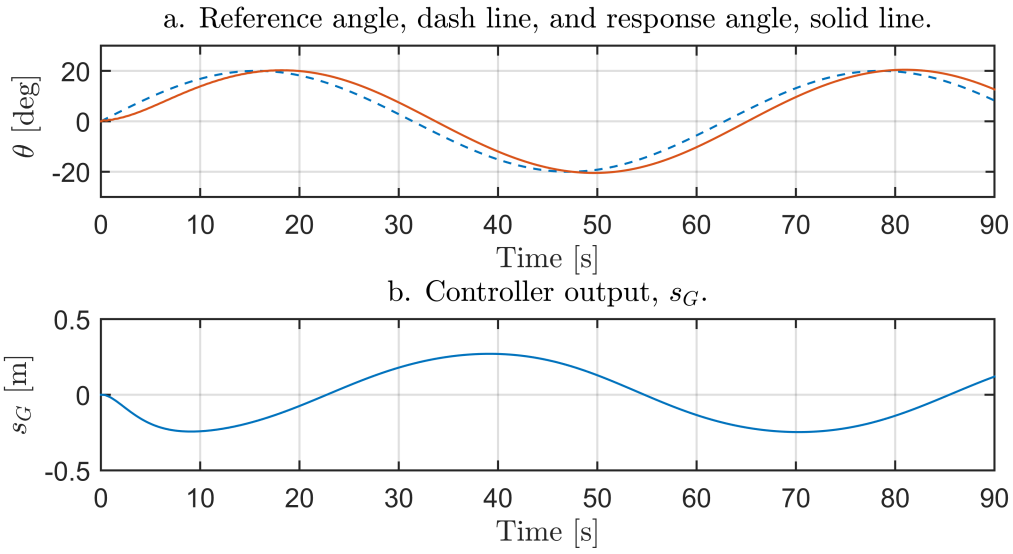

Figure 4.6: Time transition of the closed-loop simulation of the pitch angle controller with sinusoidal input and without wind disturbance.

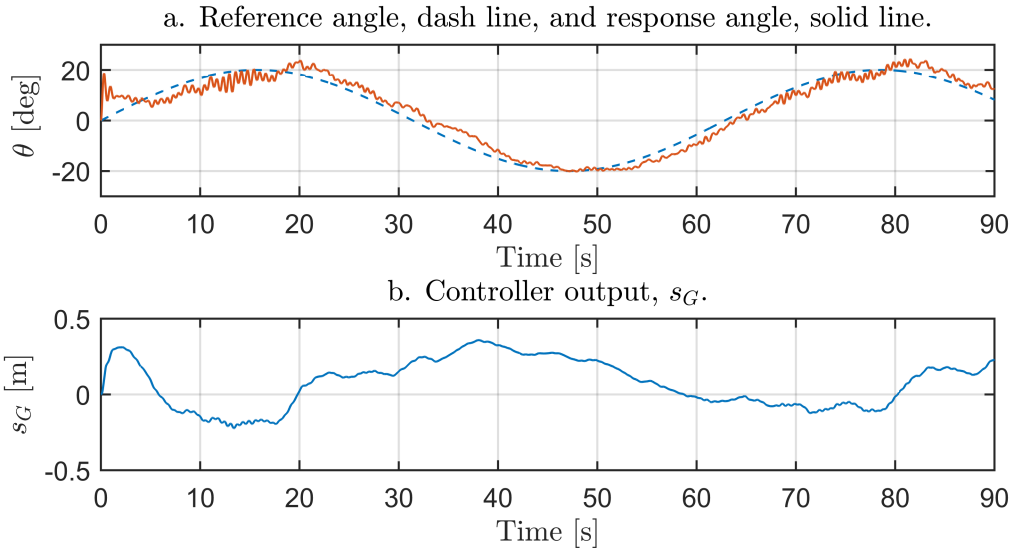

Figure 4.7: Time transition of the closed-loop simulation of the pitch angle controller with sinusoidal input and wind disturbance.

4.6-b and 4.7-b.

With no wind, the airship followed the reference pitch angle with a maximum error of 4.7°. In the case of wind, the error increased to +19° with slight oscillations for two seconds because the initial wind speed was zero and suddenly the airship was subjected to wind. As a result, the gondola moved at the fasted rate to return the airship to the reference input. Moreover, the non-constant speed and the direction of the wind resulted in oscillations between ±2° in the pitch angle as seen in figure 4.7-a while the airship was ascending.

The second reference pitch input is a square wave trajectory. The reference pitch angle is zero degree for the first thirty seconds, −20° for the second thirty seconds, and back to zero degree for the last thirty seconds. Figure 4.8 and 4.9 show plots of the simulation in the case of no wind disturbance and wind disturbance respectively. Plot 4.8-a and 4.9-a illustrate the pitch angle tracking. The controller outputs are shown in plot 4.8-b and 4.9-b.

With no wind, the error was increased to 0.77° at 4.8 s as the thrust changes from 0 to 0.2 N then the error decreased to 0.11°. The gondola moved forward at the fastest rate and remained at the saturation limit for six seconds to follow the input. The airship reached −20° in eight seconds with 5.5 % overshoot. Right before the reference of entry was changed to 0°, the tracking error was 0.56°. The airship reached zero degrees input in six seconds with 7.5 % overshoot and the error was 0.31° at 90 seconds.

The gondola position that tracks the 0^o pitch trajectory in the first 30 seconds was 0.043 m while in the last 30 seconds it was 0.15 m. The larger value of s_G is needed to maintain the higher altitude.

In the simulations with the wind, the pitch angle increased drastically at the beginning of the simulation due to its immediate application of the wind. For all tests, the gondola moved forward, and the angle returned to zero within six seconds. For the two trajectories simulated, the maximum steady state error was 3.5°.

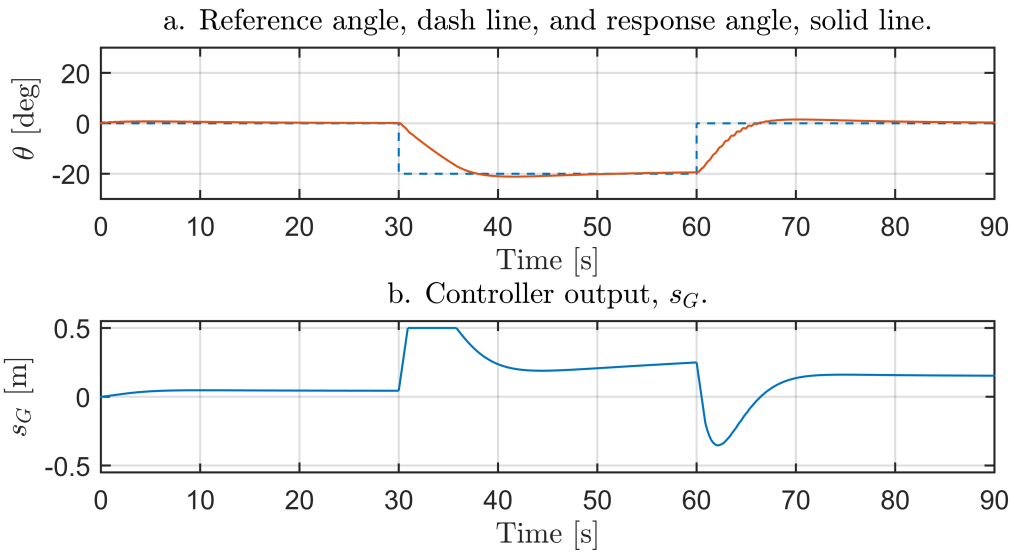

Figure 4.8: Time transition of the closed-loop simulation of the pitch angle controller with square wave input and without wind disturbance.

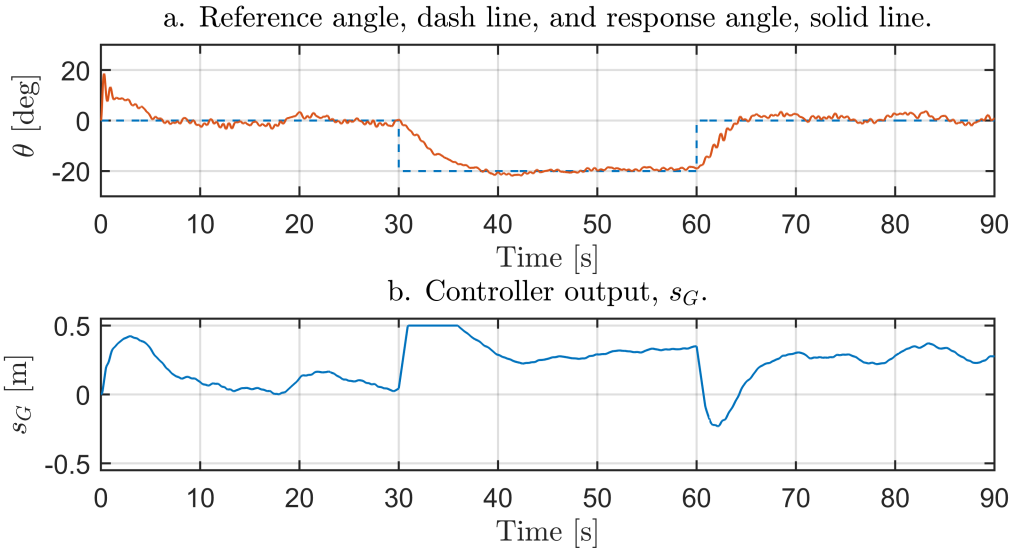

Figure 4.9: Time transition of the closed-loop simulation of the pitch angle controller with square wave input and wind disturbance.

4.4.2 Simulation results of the altitude controller

The reference input for the first altitude simulation is a sinusoidal path with a frequency of 0.10 rad/sec, an amplitude of 20 m and bias of 180 m to match the altitude of the test area. Figure 4.10 and 4.11 illustrate the closed-loop simulation of the tracking altitude and controller outputs in the case of no wind disturbance and wind disturbance, respectively. With no wind, the airship tracks the sinusoidal reference altitude with an error between -3.20 m to 4.70 m of the reference altitude. In the case of wind, the error was between -4.86 m to 4.10 m.

Similar to the second pitch trajectory, the reference input for the second altitude simulation was a square wave. The reference altitude was 180 m for the first 25 seconds, 200 m for the second 35 seconds, and 190 m for the last thirty seconds. Figure 4.12 and 4.13 show the closed-loop simulation of the tracking altitude and controller outputs in the case of no wind disturbance and wind disturbance, respectively.

With no wind, the maximum error in the first reference input was 0.71 m. The gondola moved backward at the limit gear motor speed and saturation limit to track the reference altitude. With no overshoot, the airship reached a 200 m altitude in 23 seconds. Right before the input changed to 190 m, the error was 0.10 m. Then, the airship descended to 190 m without overshooting.

With the wind, the maximum error in the first reference input was 1.4 m. The airship took 12 seconds to reach 198 m with a 2 m error. Then the error decreased slowly. Before the input changed form 200 m to 190 m, the error was -0.7 m. It took 11 seconds to reach a 1 m error. The error was decreasing, and it was -1.4 m at 90 seconds. The airship was subjected to wind from the top rear which made the altitude slower to increase and faster to decrease than the without wind case.

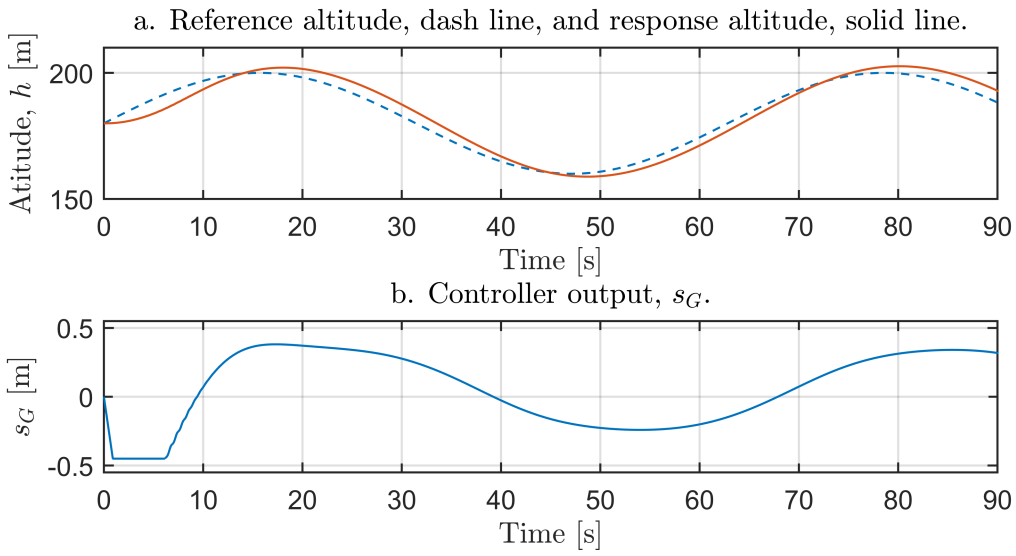

Figure 4.10: Time transition of the closed-loop simulation of the altitude controller with sinusoidal input and without wind disturbance.

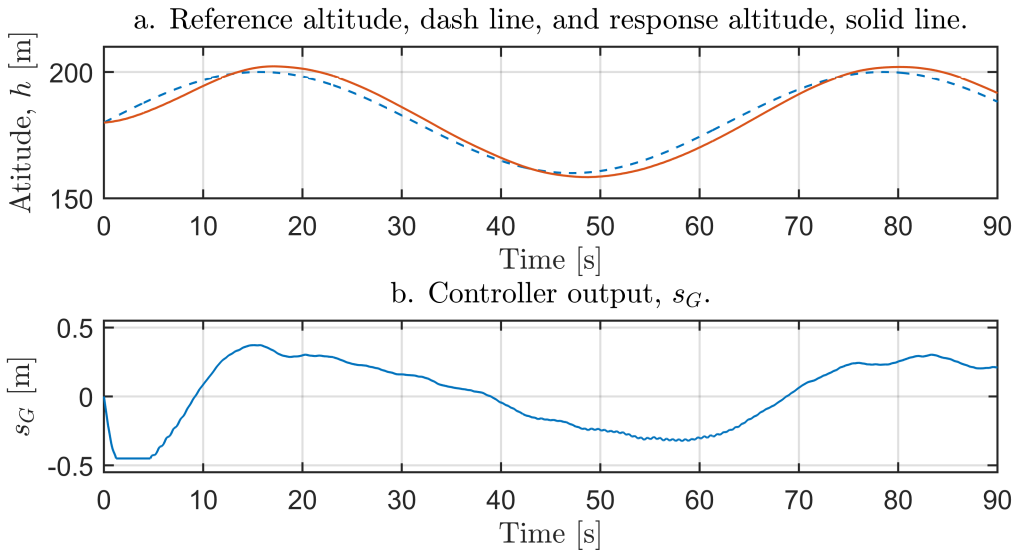

Figure 4.11: Time transition of the closed-loop simulation of the altitude controller with sinusoidal input and wind disturbance.

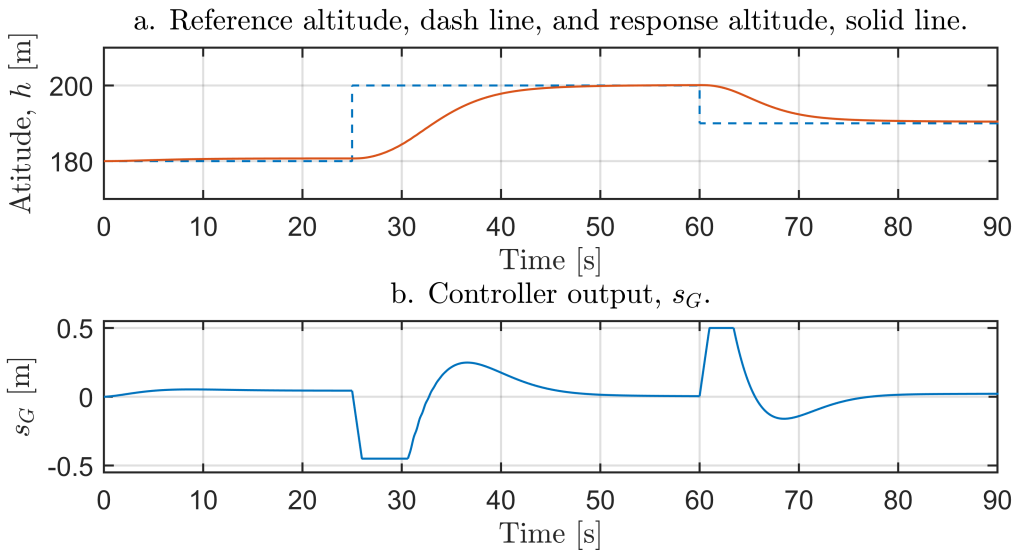

Figure 4.12: Time transition of the closed-loop simulation of the altitude controller with square wave input and without wind disturbance.

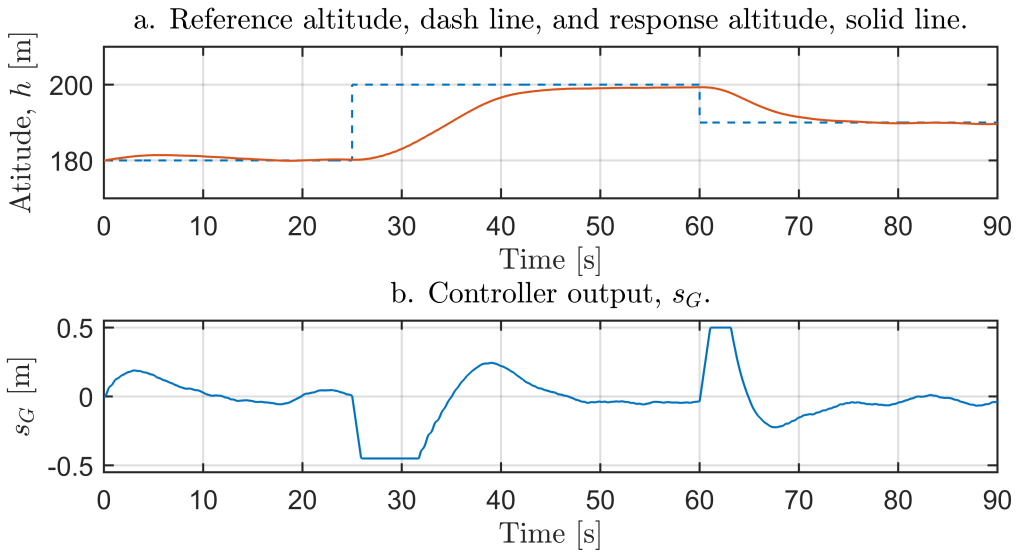

Figure 4.13: Time transition of the closed-loop simulation of the altitude controller with square wave input and wind disturbance.

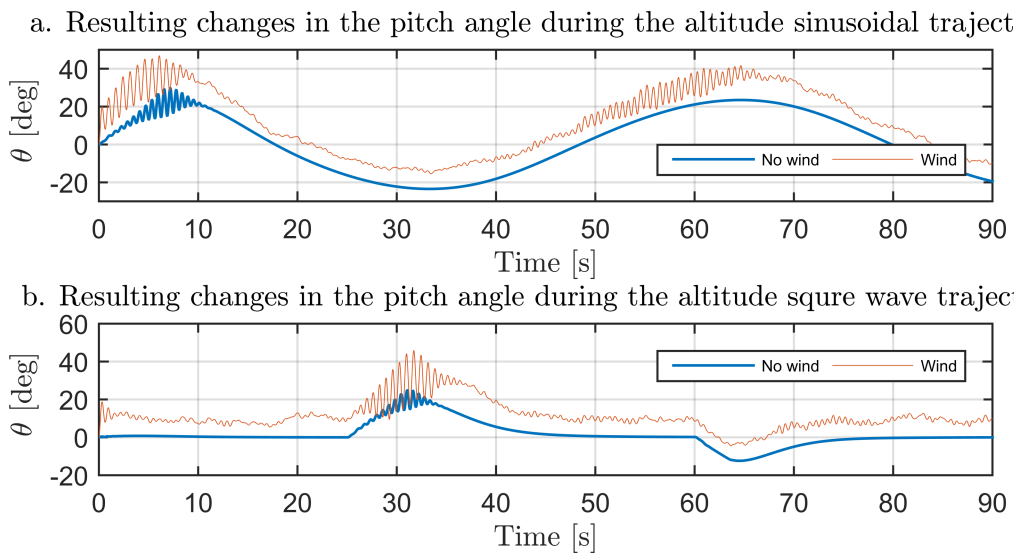

Figure 4.14: Resulting changes in the pitch angle during the altitude controller simulation in both trajectories.

The resulting changes in the pitch angle during the simulation of the altitude controller for both trajectories showed oscillation when the airship was ascending as seen in Figure 4.14.

Figure 4.14 indicates that the altitude in the wind case requires around 10 degrees more pitch angle than the no wind case to follow the same altitude trajectory through out the simulation. This is because the wind at 45 degrees induces a pitching moment as modelled in 3.46. While the wind decreased the lifting force, the increase in the pitch angle increased the lifting force and follow the same altitude in the no wind case.

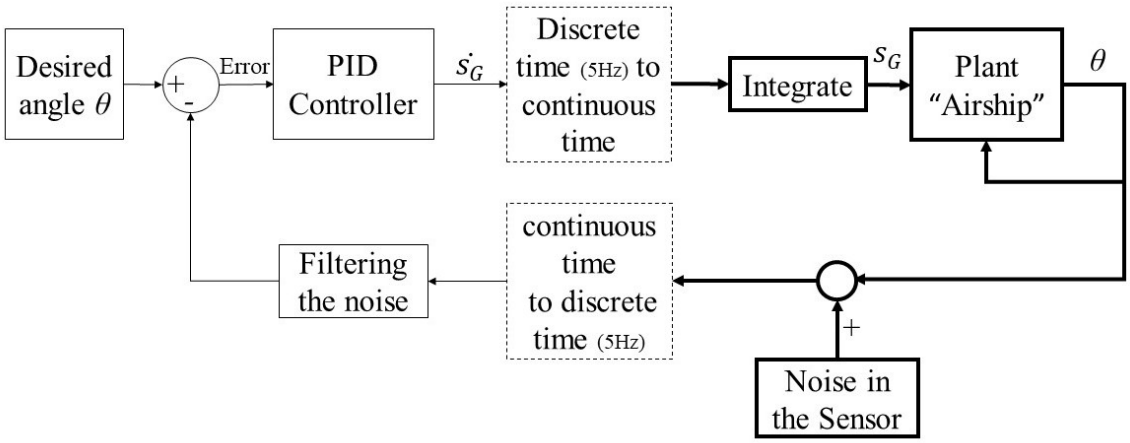

Figure 4.15: Control diagram for the experimental pitch control.

4.5 Simulation for experimental pitch control

In this section, the pitch controller is modified to respect the capabilities of the experimental platform. Figure 4.15 illustrates the control diagram for the pitch control. As it will be shown in the experimental tests, the controller output is the gondola speed $\dot{s}_G$. Moreover, noise is added to the response pitch angle. Noise can be originated from various sources such as external disturbances from the thrusters. In [55, 56], a Gaussian noise was added to all measurements from the gyroscope and the accelerometer sensors. In the simulation, the noise is derived from a Gaussian Noise with 50 variances, 0.01 sampling rate, and zero mean value. To filter the noise, a finite impulse response (FIR) digital filter was used. Many studies like in [57, 58, 59] used the FIR filter to remove the noise for the sensors. The FIR coefficients in [59] were estimated in real-time to minimize the variance of the recovered signal. The sampling rate in PID controller and the filter is 5 Hz as this represent the limitation of the ground station while it is a continuous time in the model as illustrated in Figure 4.15.

Through the simulation the thrust inputs are $T_L = T_R = 0.1$N, the elevator is $\delta_E = 0$ and rudder is $\delta_R = 0$, and they are fixed. The initial conditions of the simulation include:

1. Airship linear and angular displacements are $[x\ y\ z\ \phi\ \theta\ \psi] = [0\ 0\ 180\text{m}\ 0\ 0\ 0]$

2. Airship linear and angular velocities are $[u\ v\ w\ p\ q\ r] = [5.4\text{m/s}\ 0\ 0\ 0\ 0\ 0]$

3. Gondola position is $s_G = 0$

4. Gondola speed is $\dot{s}_G = 0$

Figure 4.16 and 4.18 show the pitch angle trajectory from the sex DOF continuous time model, from the sex DOF with applied noise, and from the discrete time model of 5 Hz with filtered noise. Figure 4.17 and 4.19 show the controller output $\dot{s}_G$ and the gondola position s_G for the test. The simulations illustrate the impacts of the vibrations and the low sampling rate on the response pitch angle and the controller performance. The average error is -0.45^{o}, and the standard deviation is 1.58^{o}. The pitch control in Section 4.4.1, that was simulated in continues time and without noises, show a steady state error of 0.1^{o} in the square wave input and 4.7^{o} in the sinusoidal input.

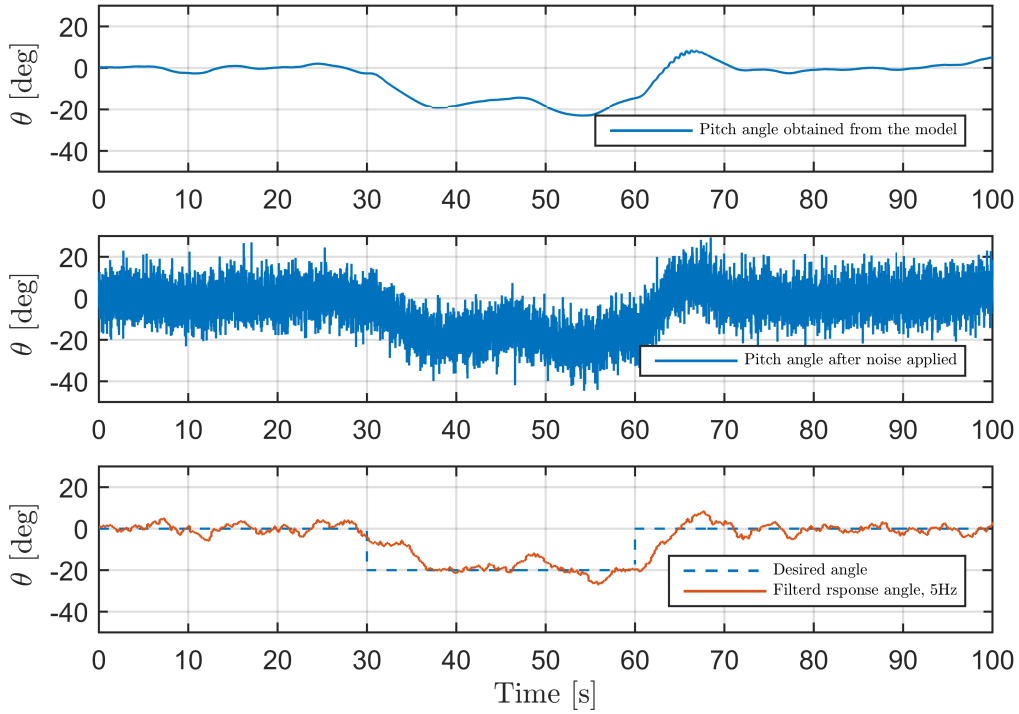

Figure 4.16: Closed-loop simulation illustrates different response pitch angle square wave input.

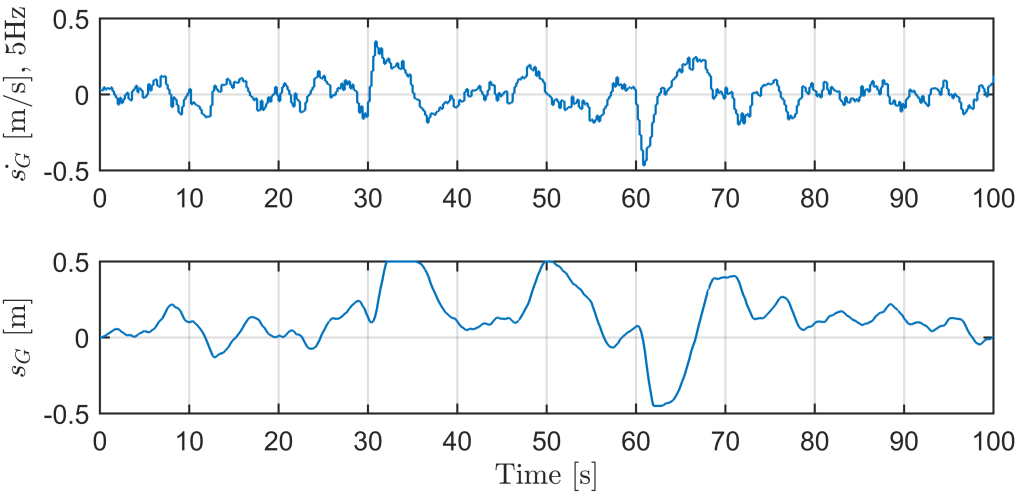

Figure 4.17: Closed-loop simulation for the experimental pitch angle control with square wave input.

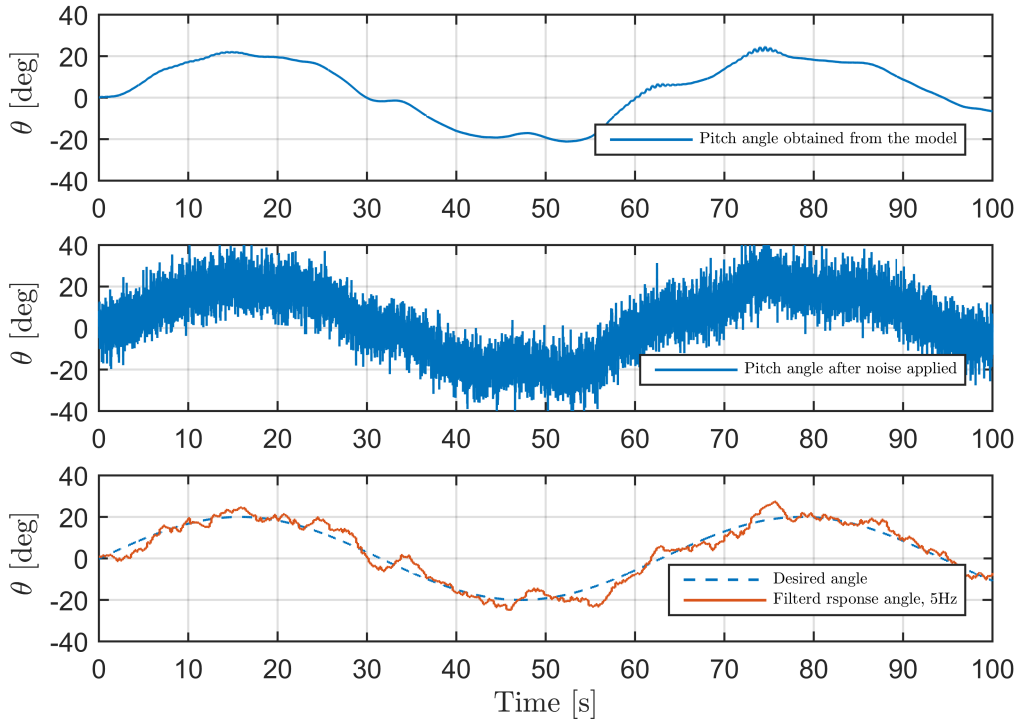

Figure 4.18: Closed-loop simulation illustrates different response pitch angle with sinusoidal input.

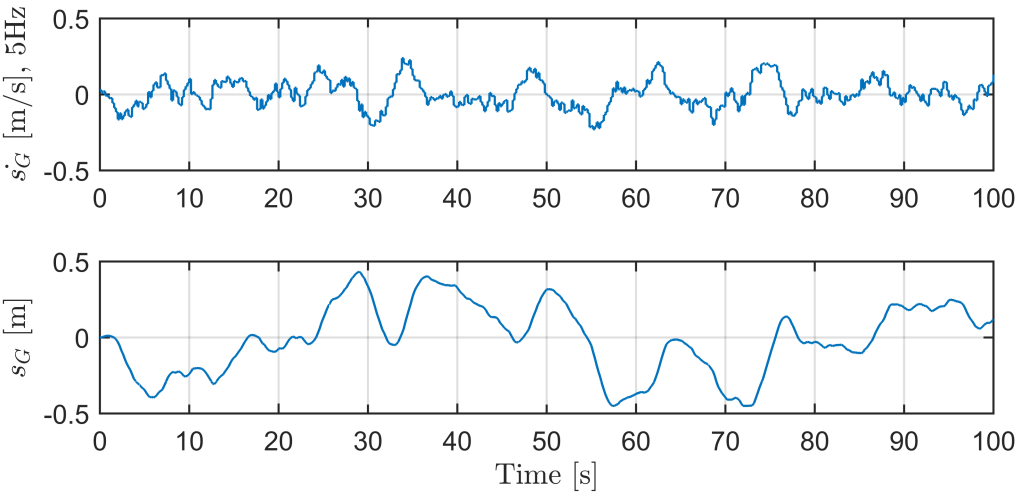

Figure 4.19: Closed-loop simulation for the experimental pitch angle control with sinusoidal input.

Chapter 5

Experimental platform

5.1 Introduction

Experimental tests were executed to validate the closed-loop PID pitch controller developed in Chapter 4. Details are provided on the experimental platform used in the test, and the computing and filtering of the pitch angle obtain from the accelerometer and gyroscopic sensors. The graphical user interface (GUI) that was designed to set the pitch trajectory and PID gains is also described.
First prototype of the gondola was developed by Dr. Lanteigne [6], Figure 5.1. It was improved for new brushless motors and sensors, Figure 5.3.

5.2 Airship design

The experimental airship is shown in Figure 5.2. The airship length is 1.83 m, volume is 0.39 m^3, and diameter is 0.6 m. The masses of the individual components of the vehicle are listed in Table 5.1. The 3D printed gondola, illustrated in Figure 5.3, is approximately 0.05 m long and can travel to the foremost position of $s_G = 0.5$ m at the bow of the airship and the rearmost position of $s_G = 0.45$ m at the stern. The gondola travels along a 4 mm x 4 mm x 1000 mm square carbon fiber keel embedded in a helium envelope. The envelope is fabricated from 2 Mil polyester polyurethane film with 90 Shore A hardness. A gear motor is used for positioning the gondola along the length of the rod. Two forward facing brushless motors that are connected to speed controllers ESCs. The airship was equipped with a Nanowii flight controller running the Multiwii open-source firmware with IMU sensor. Two long-range Bluetooth modules provide wireless communication between a Matlab/GUI in the ground and the airship. A 2 Cell, 7.4 Volt battery, was used to power the circuit. The installation diagram of the airship parts is illustrated in Figure 5.4.

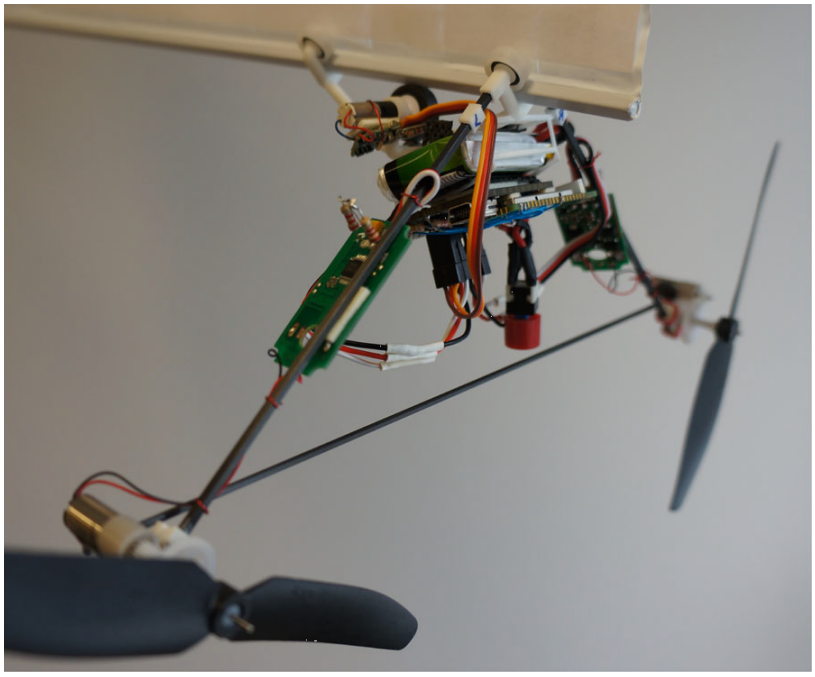

Figure 5.1: First prototype of the gondola was developed by Dr. Lanteigne [6].

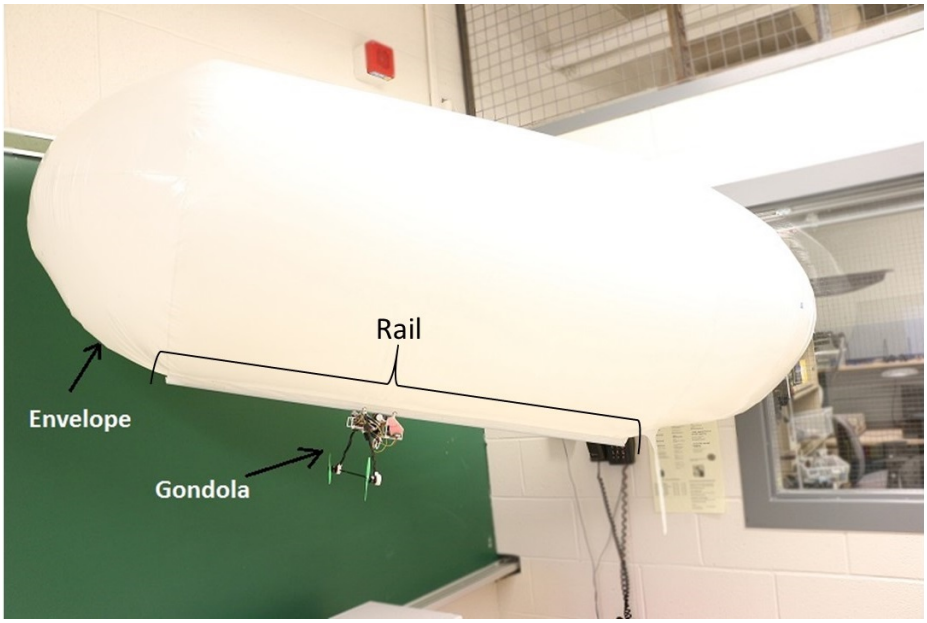

Figure 5.2: The experimental airship.

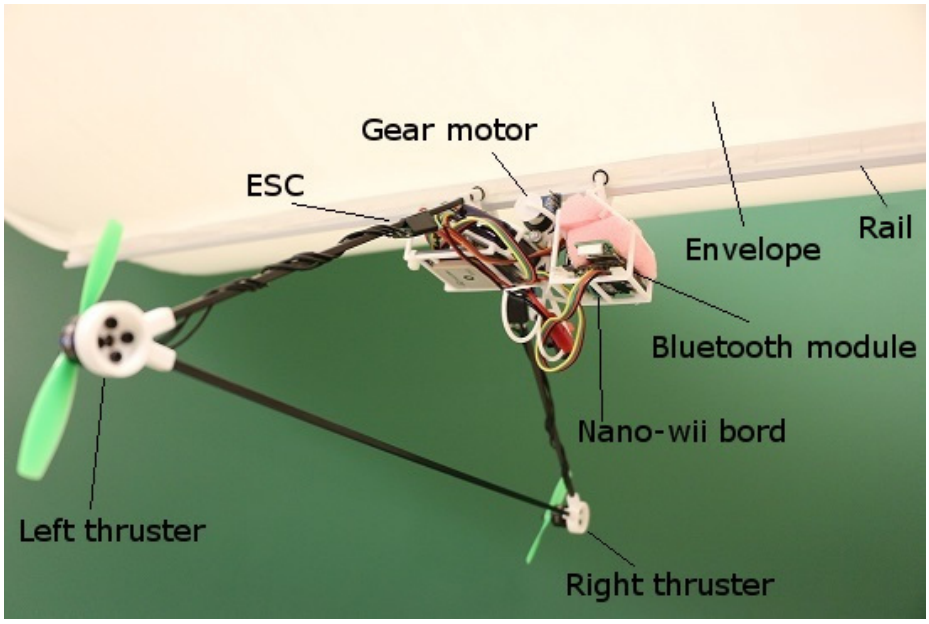

Figure 5.3: The improved gondola.

Table 5.1: Experimental airship physical properties

Symbol	Description	Value
$m_E + m_R$	Envelope and rail mass	230 g
m_G	Gondola mass	60 g
m_F	Fin mass	24 g
m_B	Ballast mass	52-105 g
V	Airship volume	0.39 m^3
L	Airship length	1.83 m
D	Airship maximum diameter	0.6 m

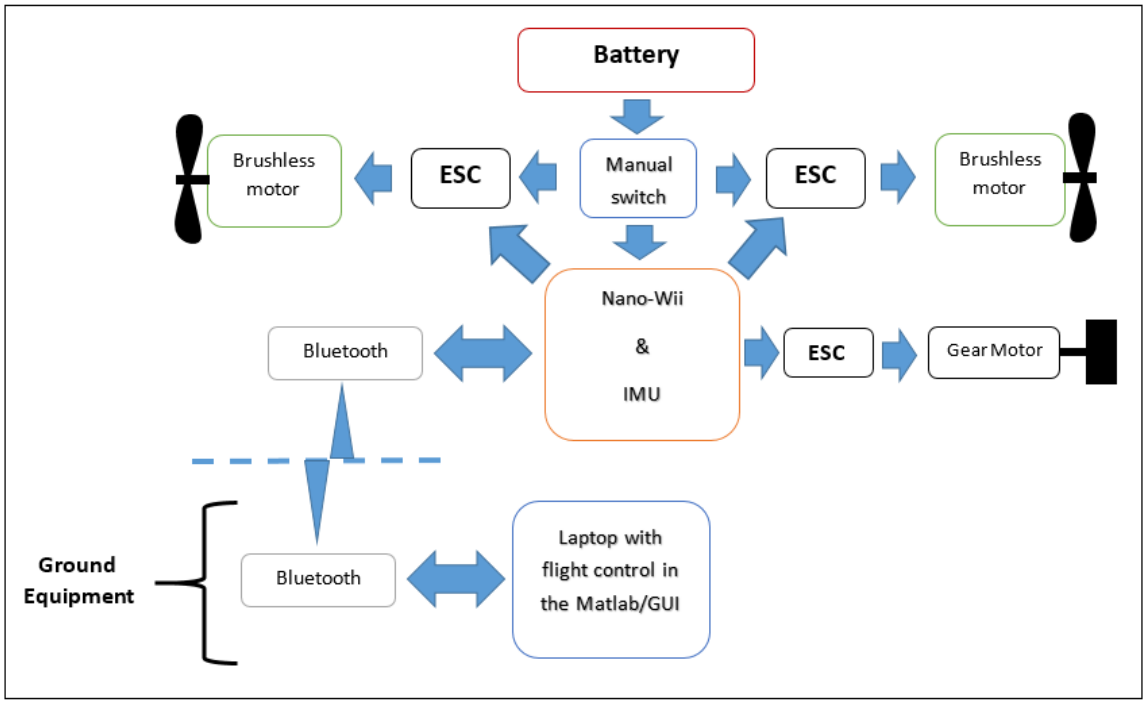

Figure 5.4: Block diagrams of the gondola onboard and PC interface.

The two motors with ESCs were tested experimentally to find the thrust versus throttle signal from the ESCs and to maintain $T = 0.1$ N from each thruster. The test setup is shown in Figure 5.5, and the test results are shown in Figure 5.6. Based on the experimental thrust characterization, the motors provide a maximum of $T_L = T_R$=0.24 N at full throttle.

5.3 Pitch angle estimation

The IMU (Inertial Measurement Unit), MPU-6050, has sex DOF from a 3-axis gyroscopic sensor and a 3-axis accelerometer. The pitch angle was obtained from the gyroscope and the accelerometer separately.

The accelerometer is highly sensitive to external disturbances like motor vibrations and its output needs to be filtered. The pitch angle θ_{acc} is computed from the accelerometer as follows:

$$\theta_{acc} = \text{atan2}(Z_{acc}, X_{acc})\frac{180}{\pi} \tag{5.1}$$

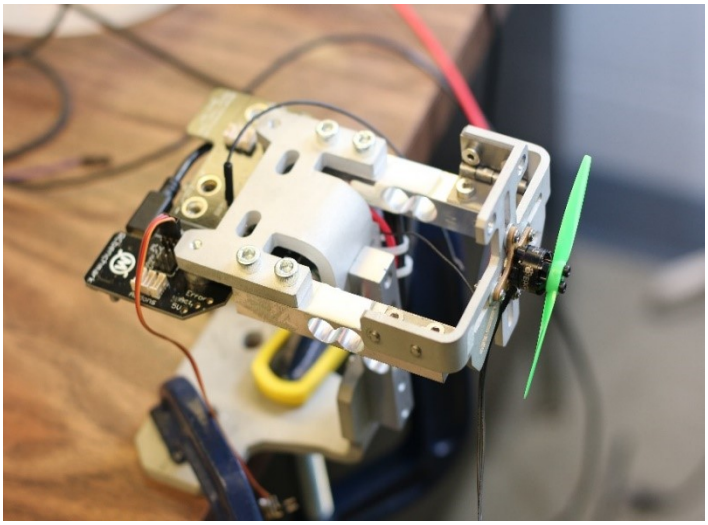

Figure 5.5: Thrust testing of the brushless motor-propeller.

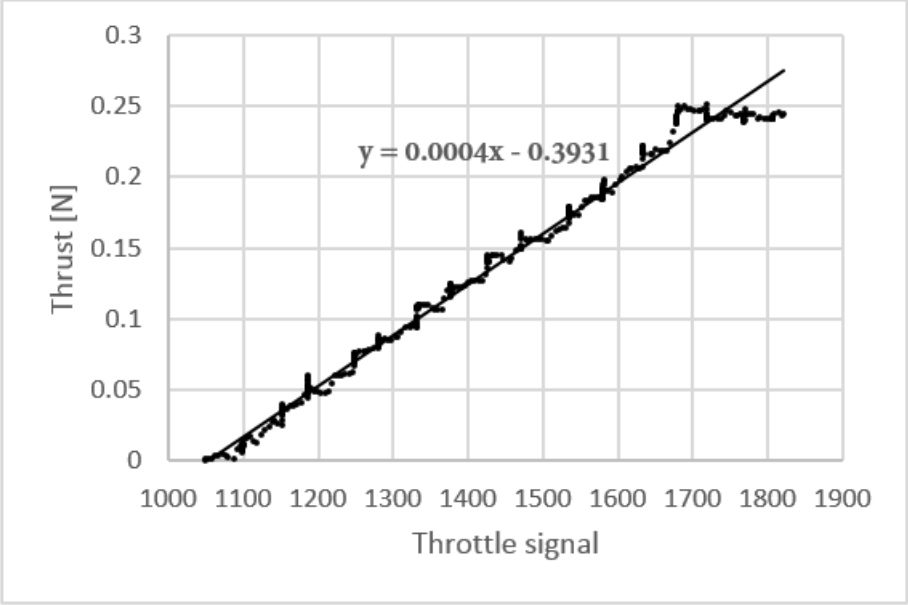

Figure 5.6: Thrust testing of the brushless motor-propeller.

where Z_{acc} and X_{acc} are the accelerometer reading of the Z and X axis, respectively.

On the other hand, the gyroscope is not subject to external forces, and the pitch rate that is measured by the gyroscope is accurate. However, the pitch angle has a tendency to drift because of the integration of the pitch rate over time. The gyroscope data is reliable only in the short term, as it quickly drifts. The pitch angle θ_{gyro} that is computed from the gyroscope is obtained as following;

$$\theta_{gyro}(t) = \frac{180}{\pi} \int_0^t \dot{\theta}_{gyro}(t)\ dt \tag{5.2}$$

where $\dot{\theta}_{gyro}(t)$ is the pitch rate from the gyroscope sensor and dt is the time step.

The complementary filter is a way of combining the accelerometer and gyroscope data. The complementary filter is very viral among hobbyists because the results are smooth and fast [60]. The complementary filter is written as following;

$$\theta = n\ (\theta + \dot{\theta}_{gyro}\ \Delta t)\ +\ (1 - n)\ \theta_{acc} \tag{5.3}$$

where n is the filter ratio and equal 0.98.

The function of the complementary filter is to ensure that the measurement will not drift in the long-term and will be accurate in the short-term by taking 98 % of the current value and adding 2 % of the angle calculated by the accelerometer.

Figure 5.7 shows plots of the pitch angle that were obtained from the gyroscope sensor θ_{gyro}, accelerometer sensor θ_{acc} and the complementary filter.

Remark 1. *the row data of the IMU was calibrated first. At a static horizontal level, the accelerometer reading has to be* $[X_{acc}\ Y_{acc}\ Z_{acc}] = [0\ 0\ 1]$ *and the gyroscope reading has to be* $[\dot{\phi}_{gyro}\ \dot{\theta}_{gyro}\ \dot{\psi}_{gyro}] = [0\ 0\ 0]$. *To remove the offset, the average of 100 reading was taken.*

5.4 Designed graphical user interface with Matlab/GUI

To assure communication between the airship and the ground computer, a graphical user interface GUI was build using Matlab/GUI. The developed GUI, shown in Figure 5.8, has several functions.

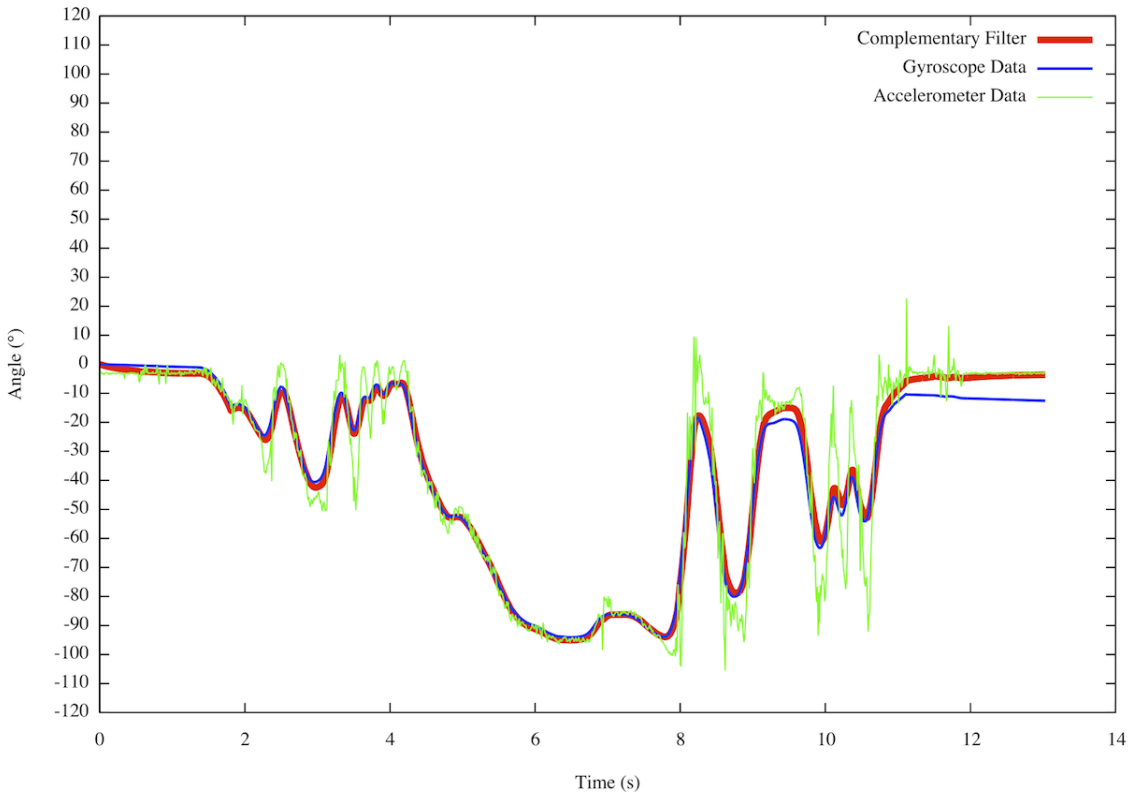

Figure 5.7: The pitch angle obtained from the complementary filter, gyroscope and accelerometer [60].

The *Connect* function initiates the communication between the Bluetooth module in the airship with the one that is connecting to the computer. Once they are connected, the refresh frequency will show and the timer will start as well as the IMU data will be received and shown in the GUI.

The *Calibrate* function is made to calibrate and remove the offset from the IMU data as described in remark 1.

The actual Pitch angle shows in the GUI in the real time, and it can be plotted as in Figure 5.9 with one-second refresh rate.

A *checkbox* function is to activate the rail motor for the gondola position and the throttle signals. A *slider* was made to send the throttle signal (1000 - 2000) the motors. The rail motor speed signal (0 - 100 %) is entered in an edit box function manually to move the gondola along the rail or the gondola runs automatically when the controller is active.

Another *checkbox* function was to activate the PID controller for the pitch angle θ. The PID controller parameters, K_p, K_i and K_d, are entered in *edit boxes* and edited anytime during the experiment as well as the desired pitch angle θ_d. Integral windup was avoided, and saturation was added to the controller output. The controller output is shown in the GUI and sent to the airship.

Another feature of the developed GUI is to save data such as time, pitch angle, desired angle, the error between real and desired pitch angles, controller output before and after saturation and the controller parameters. A push bottom named *save data* in the GUI is made to save the data to an excel sheet any time during the test named with the current date and time.

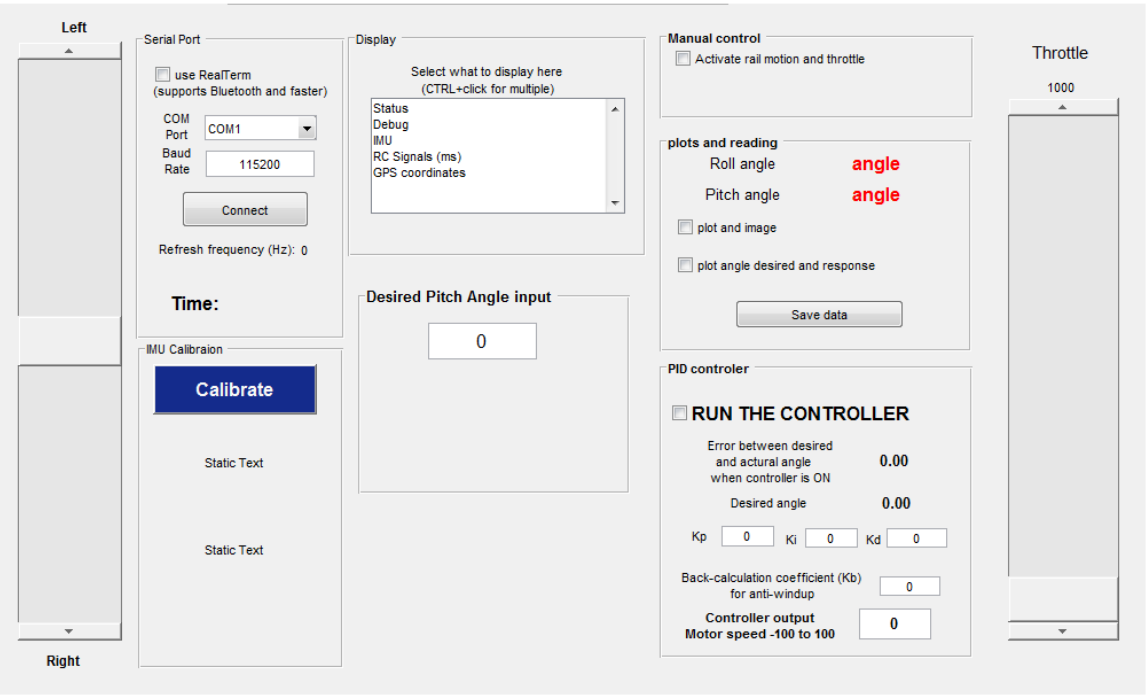

Figure 5.8: The designed GUI.

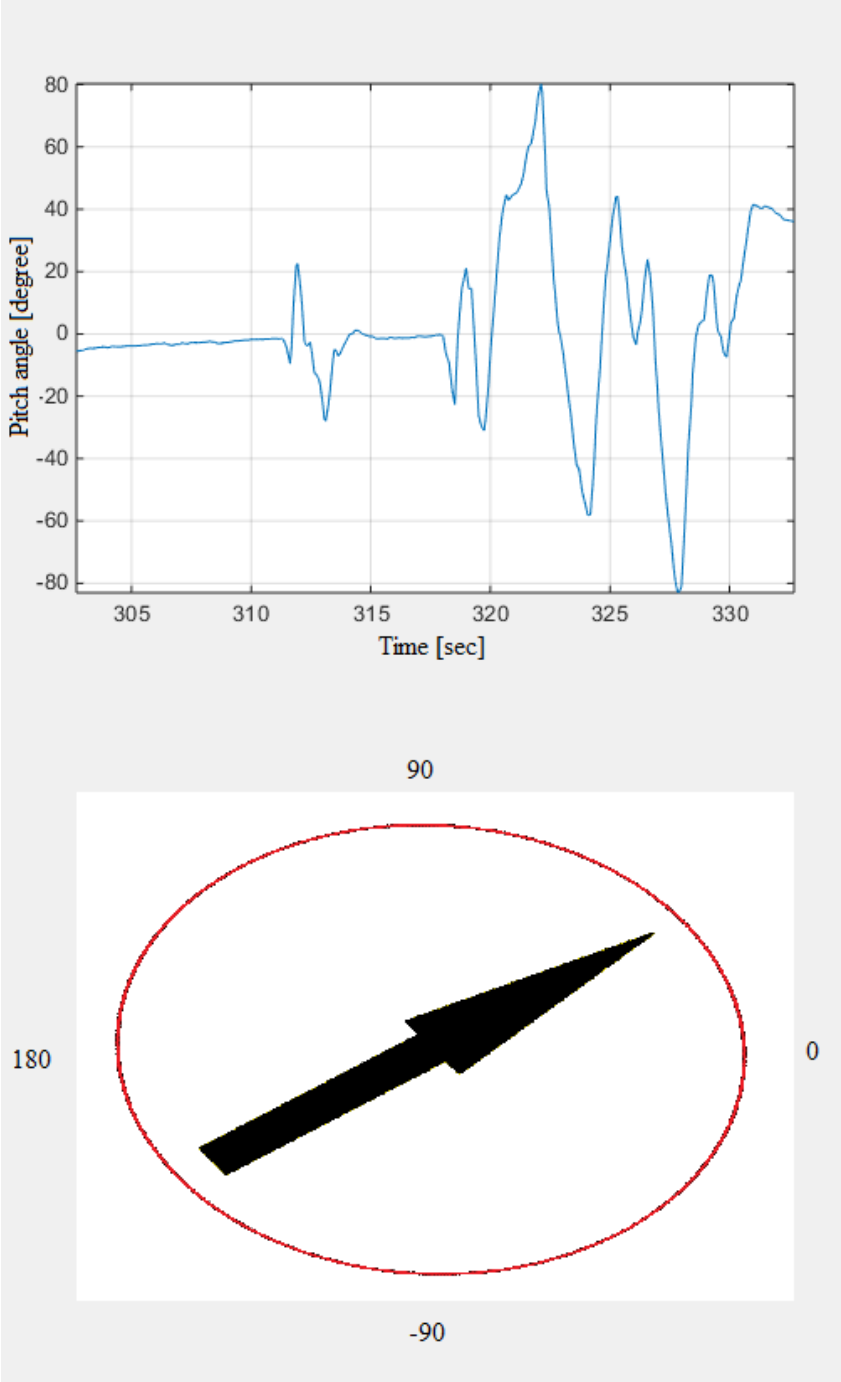

Figure 5.9: Plotting and indicator that show the pitch angle in the real time.

Chapter 6

Experimental tests and results

6.1 Introduction

In this chapter, the PID controller for pitch angle θ will be tuned first to follow the reference inputs. The controller output is the gondola speed $\dot{s}_G$ as there are no need to measure the s_G on the experimental platform. Then, the results of the flight tests will be illustrated and discussed. Figure 6.1 shows the diagram of the PID controller for the experimental test.

6.2 Tuning the PID controller for the pitch angle

The PID parameters (K_p, K_i and K_d) are directly enter in the GUI during the experiments, Figure 6.2. Ziegler-Nichols rules for tuning of PID controller parameters based on the transient response characteristics of a given plant [61]. The tuning can be made by engineers on-site by experiments on the plant. The airship exhibited unstable behaviors using the Ziegler-Nichols rules. A satisfactory performance was

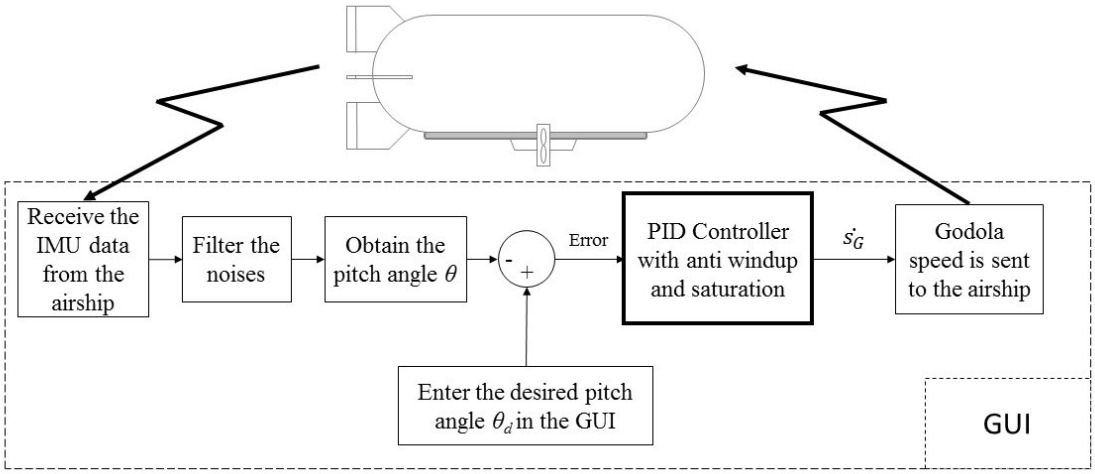

Figure 6.1: The diagram of the PID controller for the experimental test.

Table 6.1: Controller Parameters for Pitch Angle Control

Controller Parameters, PWM [%]	
K_p	-0.40
K_i	-0.10
K_d	0.20

achieved through modifying the gains that were computed in the simulation by trial and error method. The gains used for the flight tests are listed in table 6.1.

6.3 Flight tests

The flight tests were performed indoor in a hallway in Ottawa university as shown in Figure 6.3. The hallway length, height, and width are 20.3 m, 3.3 m, and 3.5 m, respectively which limited the flight tests due to the size of the hallway. The airship heading was maintained by following the vehicle and providing slight adjustments in the form of small taps on the stern of the gas envelope.

6.3.1 Flight test results of multiple step reference input

The initial speed of the airship was set to zero and the throttle was set to $T_R = T_L =$ 0.1 N using the ESC setting determined from Figure 5.6 through the flight tests. The

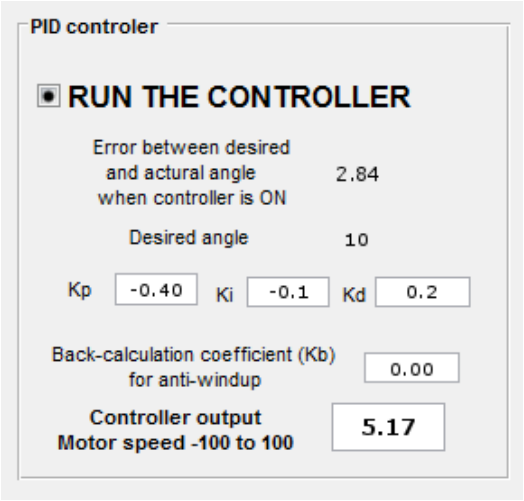

Figure 6.2: The controller section in the GUI.

Figure 6.3: Airship in test area, a hall in building 200 Lees, Ottawa university.

airship travel for about 30 seconds before reach the end of the test area. The estimated acceleration was 0.0226 m/s^2 and the estimated maximum speed was 0.68 m/s at the end of the hallway. The GUI desired pitch angle was continuously monitored to ensure that the airship did not hit the ceiling or the floor of the hallway during the tests.

The results of the flight tests for square wave reference input are illustrated in Figure 6.4 and 6.5. The figures show two reference inputs and the responses in the first plot and the controller output in the form of the gondola speed, $\dot{s}_G$ in the second plot of each figure.

Figure 6.4 shows three step reference inputs, stared at $+10°$ for 7.6 seconds then stepped down to $-10°$ for 6 seconds then stepped up to $+20°$ for 10.5 seconds then lastly stepped down to $0°$ for 7.5 seconds. The airship tracked the reference pitch angle with a maximum error between $+3°$ and $-5°$.

Figure 6.5 shows one step reference input, stared at $+20°$ for 16 seconds then stepped down to $0°$ for 21 seconds. At $+20°$ input, the airship tracked the reference pitch angle with a maximum error between $+3.5$ ° and $-4.5°$. The airship was

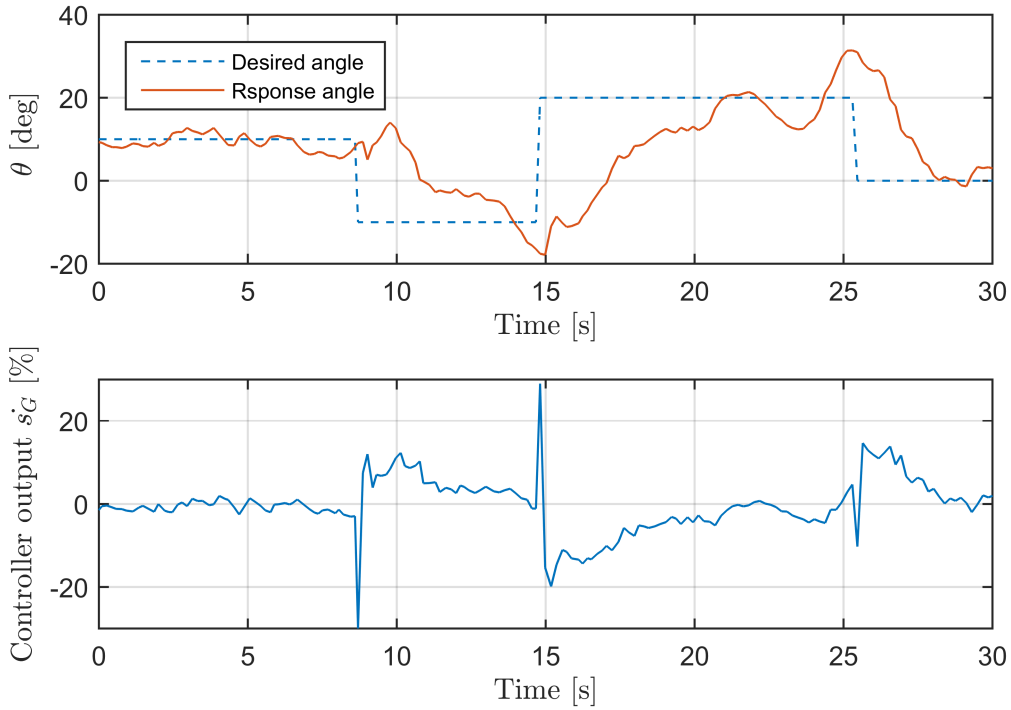

Figure 6.4: Flight test trajectory and control input with T = 0.2N.

oscillating between $+5°$ and $-6°$ around the $+0°$ input with a period of 3 seconds.

More results are shown in Figure 6.6 and 6.6. In these results, the results show that the airship took 3 to 5 seconds to reach the next step reference input. It also can clearly be seen how the controller output decreases as the pitch angle error decreases.

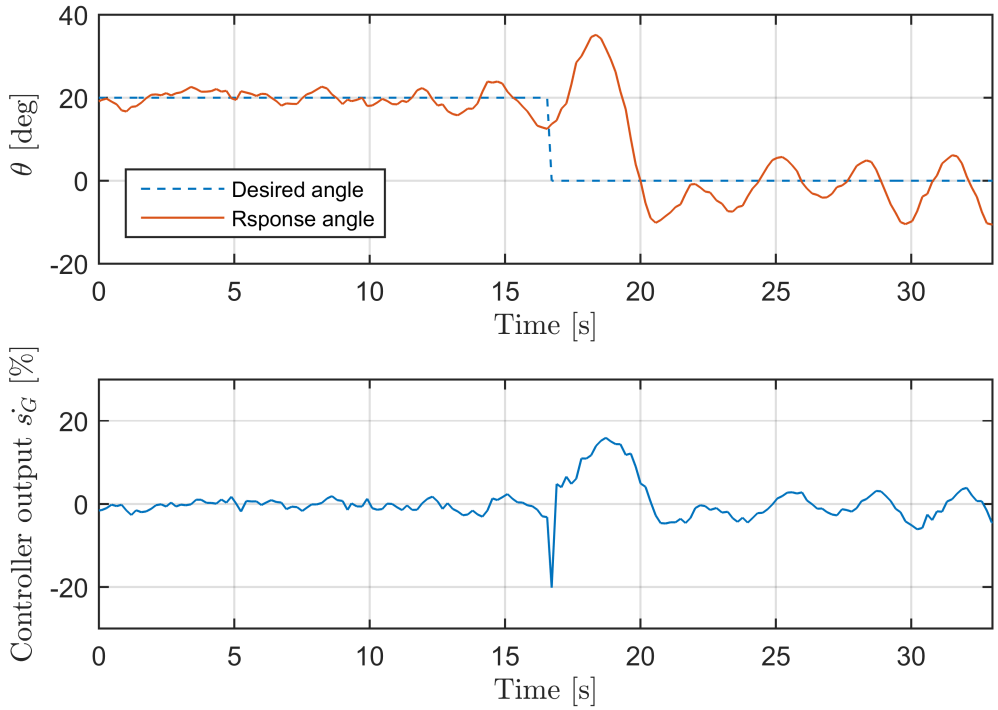

Figure 6.5: Flight test trajectory and control input with T = 0.2 N.

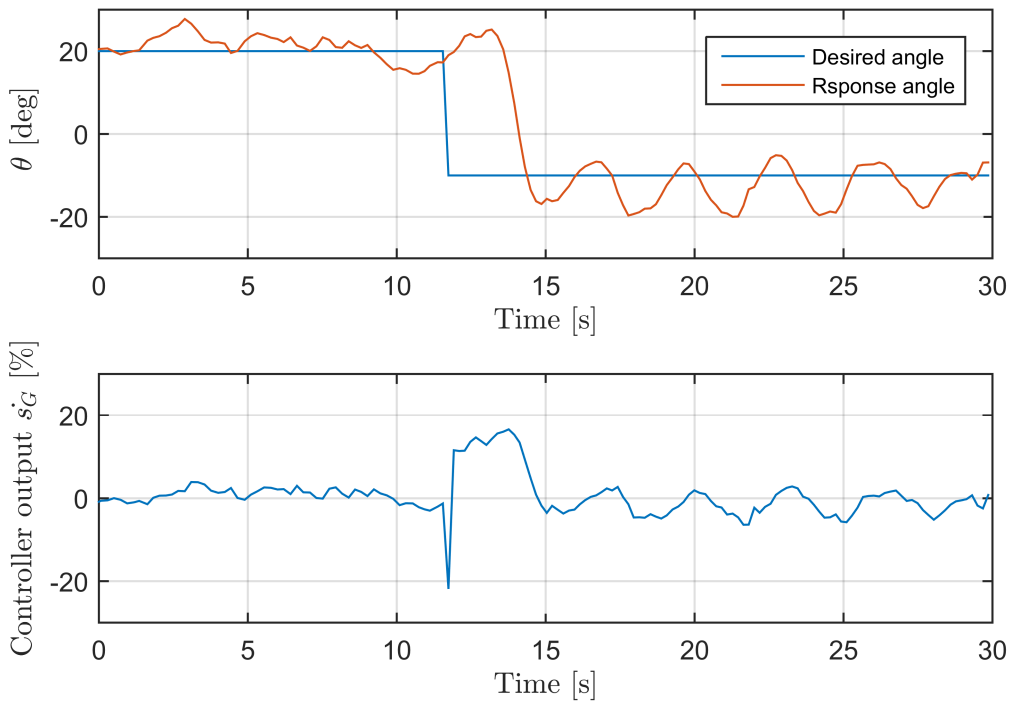

Figure 6.6: Flight test trajectory and control input with T = 0.2 N.

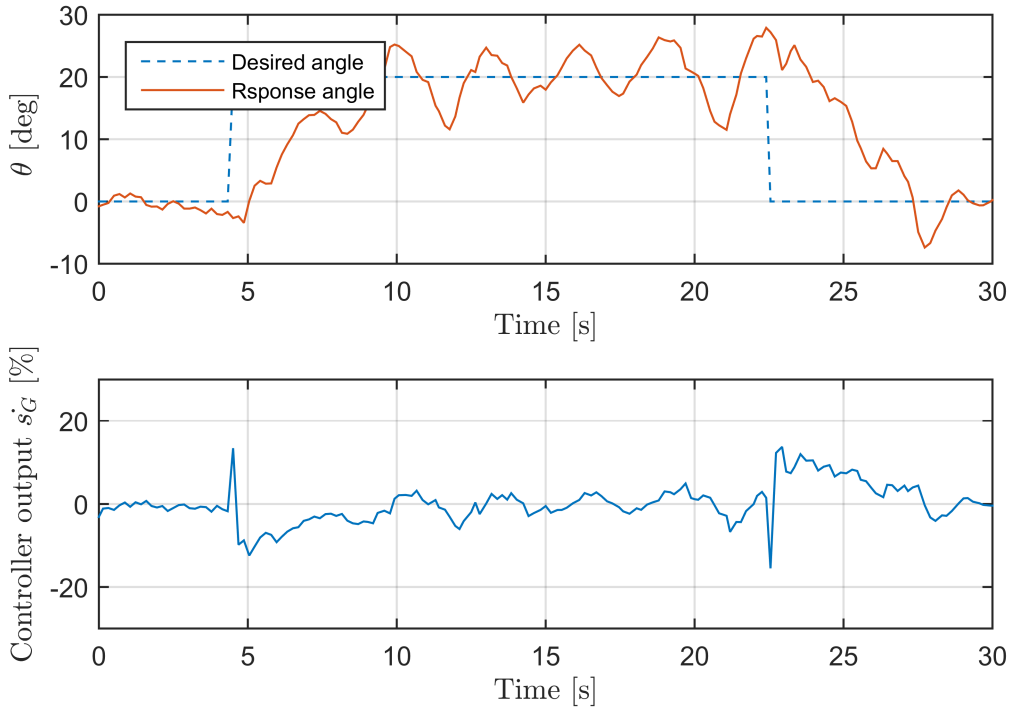

Figure 6.7: Flight test trajectory and control input with T = 0.2 N.

6.3.2 Flight test results of sinusoidal reference input

The set of tests were performed with no thruster inputs due to the length of the hallway and vibrations. The airship was set to track a sinusoidal reference input with a period of 20 second which is written as following;

$$\theta_d = 10 * \sin(\text{Time} * 20) + 5 \tag{6.1}$$

The test results are illustrated in Figure 6.8. The controller was activated after five seconds as seen by the controller output in the figure.

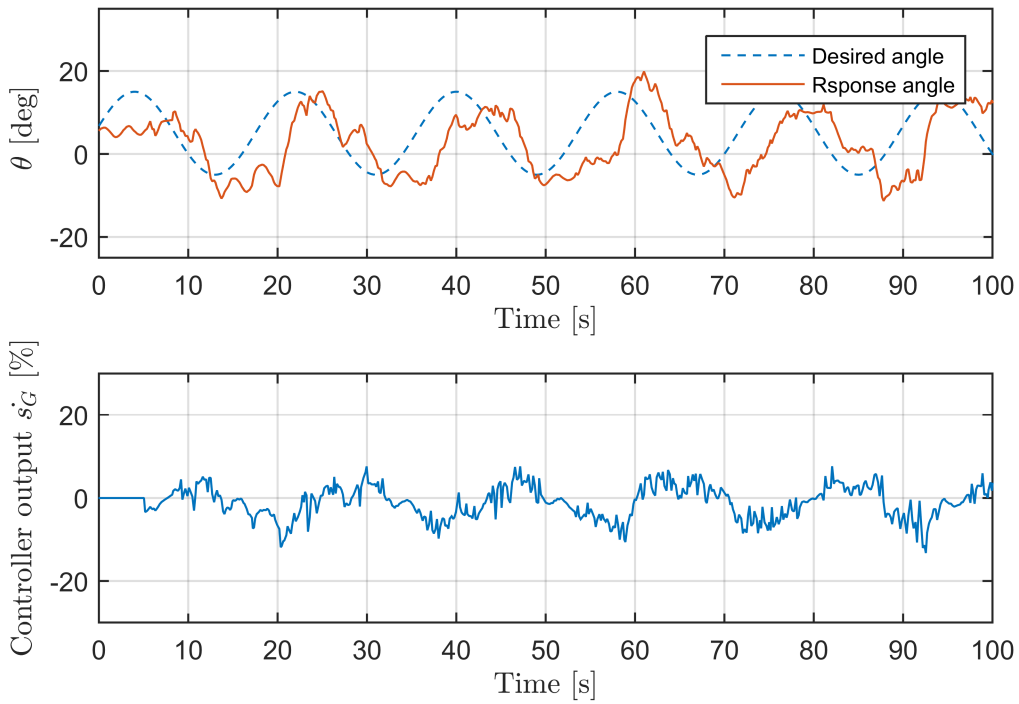

Figure 6.8: Sinusoidal pitch angle trajectory and control input with T = 0.

6.4 Discussion

Two issues affected the the estimation of the pitch angle: the sampling rate and induced vibrations. Although the data output rate of the IMU with the built in digital low pass filter could be as high as 256 Hz, the maximum GUI sampling rate was limited to 5 Hz since the control loop was implemented on the ground station to easily tune the control gains during the flight test. As a consequence approximately 98% of the IMU data was unused and the higher order plant dynamics could not be controlled. This phenomenon is easily visible from the periodic oscillations present in all test results and could be eliminated by implementing the control loop directly on the flight controller. Vibration from motors, propellers and gondola motion also add noise to the pitch angle that is obtained from the accelerometer sensor θ_{acc}. As a result of the noise, false pitch angles were computed, up to 35° while real angle was constant, as seen in Figure 6.9 between four to 32 seconds. Thus unnecessary control actions were computed by the controller. Moreover, the derivative part of

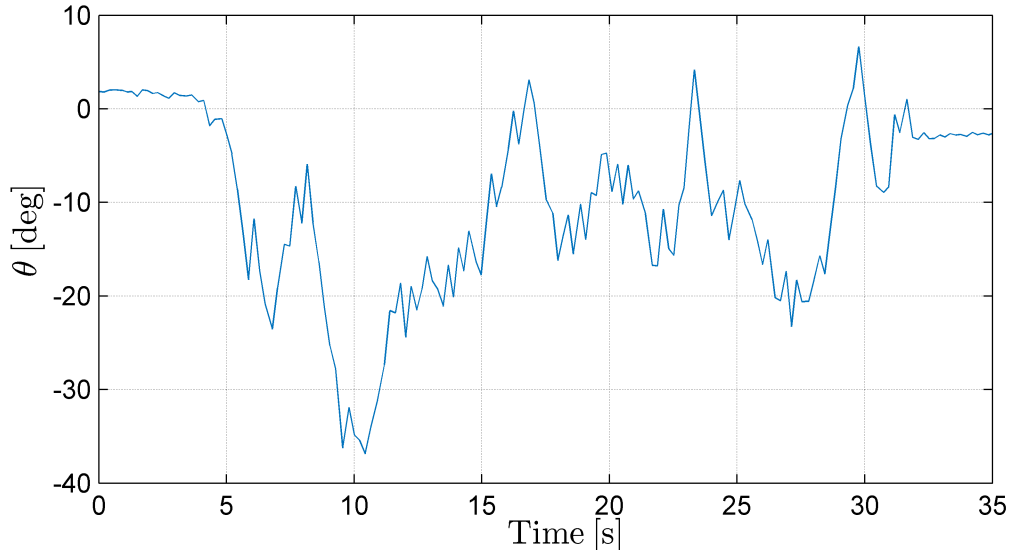

Figure 6.9: Noises in the computed pitch angle are shown between 4 to 32 seconds when the propellers are turned on.

the PID controller is quite sensitive to noise [62]. In order to reduce the noise, the IMU sensor was mounted on foam and foam rubbers were added between the motors and the frame. Moreover, the complementary filter ratio n in 5.3 was increased to 0.995, 0.5% only of the angle calculated by accelerometer. While these physical and computational limitations reduced the controllability of the vehicle, the controller could tract the reference pitch angle to within $\pm 5^{\circ}$ along straight trajectories.

Oscillations in the output pitch could also be attributed to the removal of the aileron and elevator as seen in Figure 6.3. The control surface provided significant aerodynamic pitch and yaw dumping moments having a reference area equal to approximately 35% of the enveloped reference area in the six degree of freedom as described in [6]. Figure 6.10 illustrates the longitudinal dumping moment of the envelope and the fins versus the steady state speed based on (3.46). The fins provide 19.5% of the total pitching moment. Both control surfaces were constructed of lightweight foam and had to be removed due to irreparable damage before the flight tests.

The controller output in Figure 6.4 and 6.5 shows output spikes at any change of the desired input, called the derivative kick. Figure 6.11 shows a closed-loop Simulink

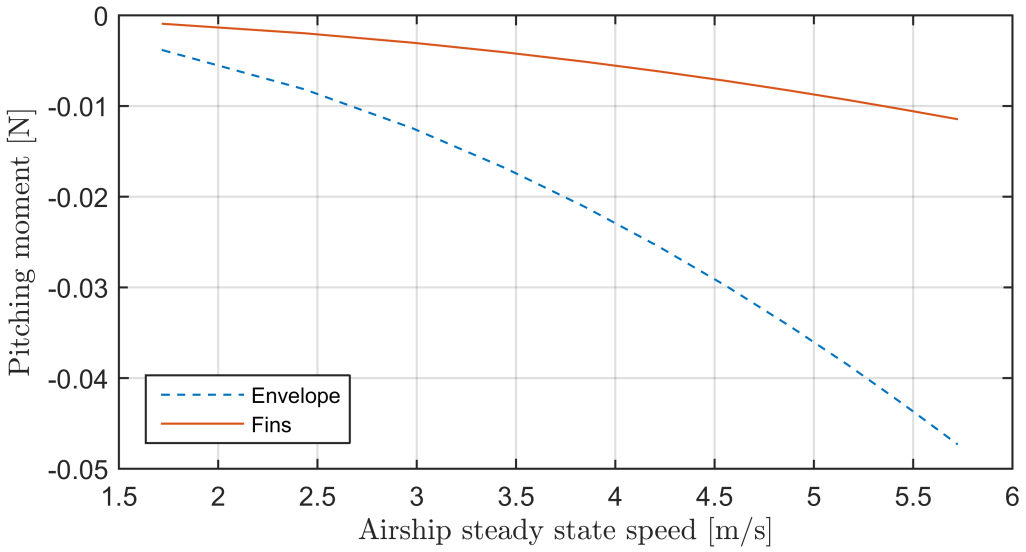

Figure 6.10: Pitching moment of the envelope and the fins at a steady state speed.

model of the longitudinal transfer function (4.16) with filtered and unfiltered PID controllers. The derivative filter can eliminate the spikes from the controller output and reduce the derivative noise on the plant output as seen in Figure 6.12.

The dimensions of the test site limited the magnitude of the reference input pitch angles and the duration of each flight test. Moreover, cold air flow through doorways and ventilation ducts introduced noticeable wind drafts along the test area.

The results of the closed-loop simulation in Section 4.5 show similarities to the flight test results in tracking error. However, the simulation shows smoother controller output and exhibit no spikes. As discussed above, the derivative term in the simulation had a derivative filter which was not implemented in the GUI.

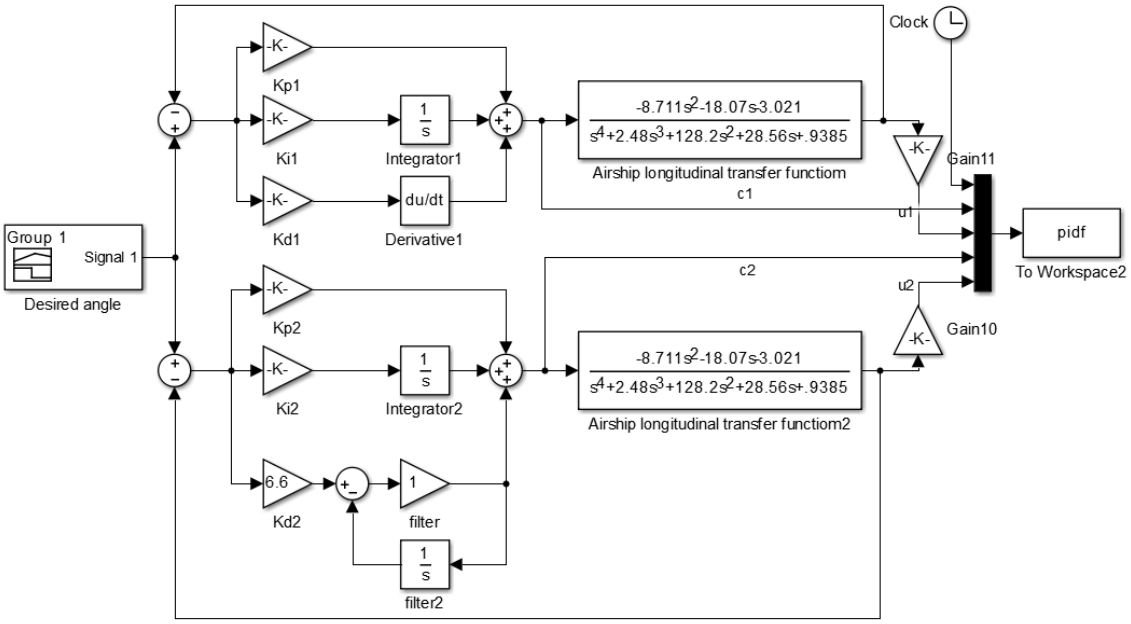

Figure 6.11: The Simulink model of the longitudinal closed-loop with two PID controllers, filtered and unfiltered.

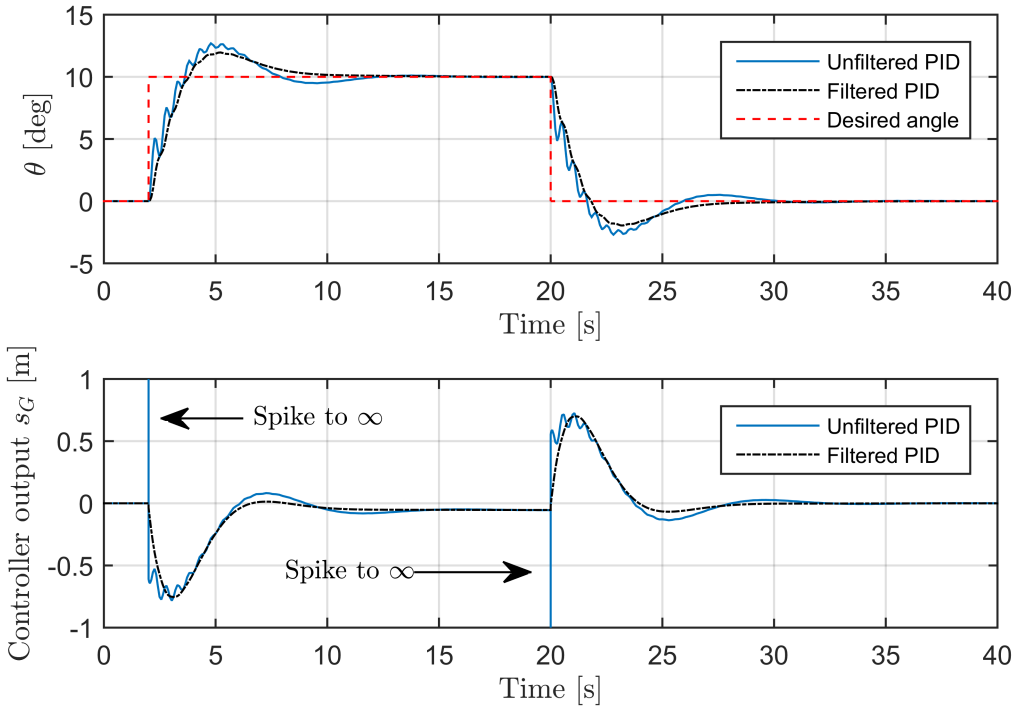

Figure 6.12: Simulation results of the closed-loop shows spikes in the controller output.

Chapter 7

Conclusion and future work

In this thesis, the six degrees of freedom equations of motion of a miniature unmanned airship with a sliding gondola was derived with the wind disturbances. Then, the model was implemented and simulated in the Matlab/Simulink. The wind disturbance was also implemented in the model. Several open-loop simulations were presented in different wind directions and thrust input. The results show the effects of the wind and the thrust on the airship pitch angle and altitude. The model was then trimmed at a zero pitch angle and constant altitude. Then, the model linearized to obtain the pitch and altitude PID controllers using the gondola position as an input. Both controllers were simulated in the Simulink with different reference inputs and the wind. Another controller was designed to respect the capabilities of the experimental platform using the gondola speed as the controller output, noises as vibrations, and low sampling rate as the ground station platform. The Simulink was an important tool for development, test, and validation of airship control systems.

The experimental platform, hardware, sensors and graphical user interface (GUI) of the ground station were described. The designed graphical user interface was able to read and control the pitch angle remotely. Then, experimental flight tests were performed to evaluate the pitch controller. The pitch angle of an experimental airship with moving gondola was controlled using a PID controller with experimentally tuned gains. The controller was able to track the desired pitch angle with a reasonable performance with the limited sampling rate of the system and the noise in the IMU generated by thruster and actuator motors. The flight test results show similarities to the simulation results in Section 4.5.

Future work includes improving the experimental platform like implement a derivative filter to the controller. The pitch angle estimation function and PID controller function will be improved if they are uploaded to the flight controller on board in the gondola instead of the GUI which has low sampling rate. Moreover, the future work

includes developing other PID controllers for takeoff and landing as it can clearly be seen in Figure 4.14 that the PID controller cannot afflictively stabilized the vehicle at large pitch angles.

References

[1] The Lyncean Group of San Diego. *Modern Airships*, August 2016 (Online; Accessed December 13, 2016). http://www.lynceans.org/all-posts/modern-airships.

[2] Y. Li. *Dynamics Modeling and Simulation of Flexible Airships*. PhD thesis, McGill Universty, 2008.

[3] Y. B. Sebbane. *Lighter than Air Robots*. Springer, 2012.

[4] M. T. Frye, S. M. Gammon, and Q. Chunjiang. The 6-dof dynamic model and simulation of the tri-turbofan remote-controlled airship. In *Proceedings of 2007 American Control Conference*, pages 816–821, July 2007.

[5] P. González, W. Burgard, R. Domínguez, and J. Fernández. Developing a low-cost autonomous indoor blimp. *Journal of Physical Agents*, 3(1):43–52, September 2009.

[6] E. Lanteigne, W. Gueaieb, D. Robillard, and S. Recoskie. Unmanned airship design with sliding ballast: Modeling and experimental validation. In *Proceedings of the 2016 International Conference on Unmanned Aircraft Systems*, pages 1246–1253, June 2016.

[7] A. Alsayed and E. Lanteigne. Experimental pitch control of an unmanned airship with sliding ballast. In *2017 International Conference on Unmanned Aircraft Systems (ICUAS)*, pages 1640–1646, June 2017.

[8] T. Liesk. *Control Design and Validation for an Unmanned, Finless Airship*. PhD thesis, McGill University, 2012.

[9] Al Arabiya English. *Saudi Arabia to use air balloon to monitor borders*, February 2017 (Online; Accessed February 14, 2017). http://english.alarabiya.net/en/News/gulf/2017/02/11/Saudi-to-use-air-balloon-to-monitor-borders.html.

[10] Hybrid Air Vehicles. *airlander 10*, (Online; Accessed February 15, 2017). https://www.hybridairvehicles.com/aircraft/airlander-10.

[11] Hybrid Air Vehicles. *Airlander Update and Review of the Year*, 2017 (Online; Accessed February 15, 2017). http://www.hybridairvehicles.com/news-and-media/news/airlander-update-and-review-of-the-year.

[12] Screenshot from YouTube. *Airship crash, Airlander 10 crashing into the ground cardington shed airship*, August 2016 (Online; Accessed February 14, 2017). https://www.youtube.com/watch?v=Mg-RPTiVa_Q.

[13] S. B. V. Gomes. *An Investigation of the Flight Dynamics of Airships with Application to the YEZ-2A*. PhD thesis, Cranfield Institute of Technology, 1990.

[14] M.Z. Ashraf and M.A. Choudhry. Dynamic modeling of the airship with matlab using geometrical aerodynamic parameters. *Aerospace Science and Technology*, 25(1):56 – 64, March 2013.

[15] B. L. Nagabhushan and N. P. Tomlinson. Flight dynamics simulation of a heavy lift airship. *Journal of Aircraft*, 18(2):96–102, February 1981.

[16] Y. Li, M. Nahon, and I. Sharf. Airship dynamics modeling: A literature review. *Progress in Aerospace Sciences*, 47(3):217 – 239, April 2011.

[17] M. B. Tischler, R. F. Ringland, and H. R. Jex. Heavy-lift airship dynamics. *Journal of Aircraft*, 20(5):425–433, May 1983.

[18] M. B. Tischler and H. R. Jex. Effects of atmospheric turbulence on a quadrotor heavy lift airship. *Journal of Aircraft*, 20(12):425–433, December 1983.

[19] The Airship Heritage Trust. *SkyShip 500*, (Accessed December 14, 2016). http://www.airshipsonline.com/airships/ss500.

[20] J. Amann. A comparison of a nonlinear flight dynamic simulation of an airship with flight test results. In *Proceedings of the 7th Lighter than Air Technology Conference*, pages 78–86, August 1987.

[21] S. P. Jones and J. D. Delaurier. Aerodynamic estimation techniques for aerostats and airships. *Journal of Aircraft*, 2(2):120–126, February 1983.

[22] Y. Li and M. Nahon. Modeling and simulation of airship dynamics. *Journal of Guidance, Control, and Dynamics*, 30(6):1691–1700, November-December 2007.

[23] H. Jex, R. Magdaleno, P. Gelhausen, and M. Tischler. Pre- and post-flight-test models versus measured skyship-500 control responses. In *Proceedings of the 7th Lighter than Air Technology Conference*, pages 87–97, August 1987.

[24] P. G. Thomasson. Equations of motion of a vehicle in a moving fluid. *Journal of Aircraft*, 37(4):630–639, July 2000.

[25] J. R. Azinheira, E. Carneiro de Paiva, and S. S. Bueno. Influence of wind speed on airship dynamics. *Journal of Guidance, Control, and Dynamics*, 25(6):1116–1124, November-December 2002.

[26] P. Peddiraju, T. Liesk, and M. Nahon. Dynamics modeling for an unmanned, unstable, fin-less airship. In *Proceedings of the 18th AIAA Lighter-Than-Air Systems Technology Conference*, May 2009.

[27] X. Wang, Z. Zuo, and C. Liu. Three dimensional path-following control of an under-actuated airship. In *Chinese Control Conference, CCC*, volume 2016-Augus, pages 4627–4632. IEEE, jul 2016.

[28] Z. Zheng and Y. Zou. Adaptive integral LOS path following for an unmanned airship with uncertainties based on robust RBFNN backstepping. *ISA Transactions*, 65:210–219, nov 2016.

[29] S. Q. Liu, S. J. Gong, Y. X. Li, and Z. R. Lu. Vectorial backstepping method–based trajectory tracking control for an under–actuated stratospheric airship. *The Aeronautical Journal*, 121(916):916–939, 2017.

[30] G. A. Khoury. *Airship technology*. Cambridge University Press, 2012.

[31] C. Hong, K. Choi, and B. Kim. Applications of adaptive neural network control to an unmanned airship. *International Journal of Control, Automation and Systems*, 7(6):911–917, December 2009.

[32] W. Adamski, P. Herman, Y. Bestaoui, and K. Kozłowski. Control of airship in case of unpredictable environment conditions. In *Proceedings of the Control and Fault-Tolerant Systems*, pages 843–848, October 2010.

[33] E. Carneiro de Paiva, S. S. Bueno, S. B. V. Gomes, J. J. G. Ramos, and M. Bergerman. A control system development environment for aurora's semi-autonomous robotic airship. In *Proceedings of the 1999 IEEE International Conference on Robotics & Automation*, volume 3, pages 2328–2335, May 1999.

[34] J. R. Azinheira, A. Moutinho, and E. Carneiro de Paiva. A backstepping controller for path-tracking of an underactuated autonomous airship. *International Journal of Robust and Nonlinear Control*, 19(4):418–441, March 2009.

[35] S. Recoskie. *Autonomous Hybrid Powered Long Ranged Airship For Surveillance and Guidance*. PhD thesis, Ottawa Universty, 2014.

[36] T. Liesk, M. Nahon, and B. Boulet. Design and experimental validation of a nonlinear low-level controller for an unmanned fin-less airship. *IEEE Transactions on Control Systems Technology*, 21(1):149–161, January 2013.

[37] Y. Yang, J. Wu, and W. Zheng. Adaptive fuzzy sliding mode control for robotic airship with model uncertainty and external disturbance. *Journal of Systems Engineering and Electronics*, 23(2):250–255, April 2012.

[38] Y. Yang, J. Wu, and W. Zheng. Attitude control for a station keeping airship using feedback linearization and fuzzy sliding mode control. *International Journal of Innovative Computing, Information and Control*, 8(12):8299–8310, December 2012.

[39] E. Kahale, P. C. Garcia, and Y. Bestaoui. Autonomous path tracking of a kinematic airship in presence of unknown gust. *Journal of Intelligent & Robotic Systems*, 69(1):431–446, January 2013.

[40] R. V. B. Henriques, J. R. Azinheira, A. Moutinho, and J. R. Carvalho. Lateral control of airship with uncertain dynamics using incremental nonlinear dynamics inversion. In *Proceedings of the 11th IFAC Symposium on Robot Control*, volume 48, pages 69 – 74, August 2015.

[41] Z. Zheng, W. Huo, and Z. Wu. Trajectory tracking control for underactuated stratospheric airship. *Advances in Space Research*, 50(7):906–917, October 2012.

[42] R. Fedorenko and V. Krukhmalev. Indoor autonomous airship control and navigation system. In *Proceedings of the 3rd International Conference on Control, Mechatronics and Automation*, volume 42, pages 1–6, February 2016.

[43] Y. Liu, Z. Pan, D. Stirling, and F. Naghdy. Control of autonomous airship. In *Proceedings of the Robotics and Biomimetics*, pages 2457–2462, December 2009.

[44] E. C. de Paiva, S. S. Bueno, and M. Bergerman. A Robust Pitch Attitude Controller for Aurora's Semi-Autonomous Robotic Airship. (c):141–148, 1999.

[45] A. Elfes, J. F. Montgomery, J. Hall, S. Joshi, J. Payne, and C. Bergh. Autonomous Flight Control for a Planetary Exploration Aerobot. *Space 2005*, pages 1–9, 2005.

[46] H. Mazhar. Dynamics , Control and Flight Testing of an Unmanned , Finless Airship. (December), 2012.

[47] S. B. V. Gomes and J. J. G. Ramos. Airship dynamic modeling for autonomous operation. In *Proceedings of the Robotics and Automation*, volume 4, pages 3462–3467. IEEE, May 1998.

[48] G. C. Avenant. *Autonomous Flight Control System for an Airship*. PhD thesis, Stellenbosch University, 2010.

[49] H. Lamb. The inertia coefficients of an ellipsoid moving in fluid. Technical report, British Aeronautical Research Commitee, 1918.

[50] M. M. Munk. Aerodynamics of airships. *Aerodynamic Theory*, 6:32–48, 1936.

[51] J. B. Mueller, M. A. Paluszek, and Y. Zhao. Development of an aerodynamic model and control law design for a high altitude airship. In *Proceedings of the 3rd Unmanned Unlimited Technical Conference*, pages 1–17, September 2004.

[52] S. F. Hoerner. *Fluid dynamic Drag*. Hoerner Fluid Dynamics, 1965.

[53] D. P. Raymer. *Aircraft Design: A Conceptual Approach*. Amer Institute of Aeronautics, 2012.

[54] T. Hägglund. Signal filtering in pid control. In *Proceedings of 2nd IFAC Conference on Advances in PID Control*, volume 45, pages 1–10, 2012.

[55] L. Fusini, T. A. Johansen, and T. I. Fossen. Dead reckoning of a fixed-wing uav with inertial navigation aided by optical flow. In *2017 International Conference on Unmanned Aircraft Systems (ICUAS)*, pages 1250–1259, June 2017.

[56] B. Pugach, B. Beallo, D. Bement, S. McGough, N. Miller, J. Morgan, L. Rodriguez, K. Winterer, T. Sherman, S. Bhandari, and Z. Aliyazicioglu. Nonlinear controller for a uav using echo state network. In *2017 International Conference on Unmanned Aircraft Systems (ICUAS)*, pages 124–132, June 2017.

[57] S. Pannu and R. Horowitz. Adaptive accelerometer feedforward servo for disk drives. In *Proceedings of the 36th IEEE Conference on Decision and Control*, volume 5, pages 4216–4218 vol.5, Dec 1997.

[58] M. J. Mathie, N. H. Lovell, A. C. F. Coster, and B. G. Celler. Determining activity using a triaxial accelerometer. In *Proceedings of the Second Joint 24th Annual Conference and the Annual Fall Meeting of the Biomedical Engineering Society] [Engineering in Medicine and Biology*, volume 3, pages 2481–2482 vol.3, Oct 2002.

[59] H. H. Asada, Hong-Hui Jiang, and P. Gibbs. Active noise cancellation using mems accelerometers for motion-tolerant wearable bio-sensors. In *The 26th Annual International Conference of the IEEE Engineering in Medicine and Biology Society*, volume 1, pages 2157–2160, Sept 2004.

[60] P. Van de Maele. *Reading a IMU Without Kalman: The Complementary Filter*, January 2013 (Online; Accessed February 17, 2017). http://www.pieter-jan.com/node/11.

[61] K. Ogata. *Modern control engineering*. Prentice-Hall, Inc., 3rd edition, 1997.

[62] J. Hellerstein. *Feedback control of computing systems*. IEEE Press, 2004.